Constraining the Exozodiacal Luminosity Function of Main Sequence Stars: Complete Results from the Keck Nuller Mid-Infrared Surveys

B. Mennesson[1], R. Millan-Gabet[2], E. Serabyn[1], M. M. Colavita[1], O. Absil[3], G. Bryden[1], M. Wyatt[4], W. Danchi[5], D. Defrère[6], O. Doré[1], P. Hinz[6], M. Kuchner[5], S. Ragland[7], N. Scott[8], K. Stapelfeldt[5], W. Traub[1], J. Woillez[9]

ABSTRACT

Forty-seven nearby main sequence stars were surveyed with the Keck Interferometer mid-infrared Nulling instrument (KIN) between 2008 and 2011, searching for faint resolved emission from exozodiacal dust. Observations of a subset of the sample have already been reported, focusing essentially on stars with no previously known dust (Millan-Gabet et al. 2011, hereafter Paper I). Here we extend this analysis to the whole KIN sample, including 22 more stars with known near- and/or far-infrared excesses. In addition to an analysis similar to that of Paper I, which was restricted to the 8 to 9 μm spectral region, we present measurements obtained in all 10 spectral channels covering the 8 to 13 μm instrumental bandwidth. Based on the 8 to 9 μm data alone, which provide the highest signal to noise measurements, only one star shows a large excess imputable to dust emission (η Crv), while 4 more show a significant ($> 3\sigma$) excess: β Leo, β UMa, ζ Lep and γ Oph. Overall, excesses detected by KIN are more frequent around A-type stars than later spectral types. A statistical analysis of the measurements further indicates that stars with known far-infrared ($\lambda \geq 70$ μm) excesses have higher exozodiacal emission levels than stars with no previous indication of a cold outer disk. This statistical trend is observed regardless of spectral type and points to a dynamical connection between the inner (zodi-like) and outer (Kuiper belt like) dust populations. The measured levels for such stars are clustering close to the KIN detection limit of a few 100 zodis and are indeed consistent with those expected from a population of dust that migrated in from the outer belt by Poynting-Robertson drag. Conversely, no significant mid-infrared excess is found around sources with a previously reported near-infrared resolved excess, which typically have levels of the order of 1% over the photospheric flux. If dust emission is really at play in these near-infrared detections, the absence of a strong

[1]Jet Propulsion Laboratory, California Institute of Technology, 4800 Oak Grove Drive, Pasadena CA 91109-8099, USA

[2]NASA Exoplanet Science Center, California Institute of Technology, 770 South Wilson Avenue, Pasadena CA 91125, USA

[3]Département d'Astrophysique, Géophysique et Océanographie, Université de Liège, 17 Allée du Six Août, 4000 Liège, Belgium

[4]Institute of Astronomy, University of Cambridge, Madingley Road, Cambridge CB3 0HA, UK

[5]NASA Goddard Space Flight Center, Exoplanets and Stellar Astrophysics Laboratory, Code 667, Greenbelt, MD 20771, USA

[6]Steward Observatory, University of Arizona, 933 N Cherry Avenue,Tucson, AZ 85721, USA

[7]Keck Observatory, 65-1120 Mamalahoa Hwy, Kamuela, HI 96743, USA

[8]Center for High Angular Resolution Astronomy, Georgia State University, Mt. Wilson, CA 91023, USA

[9]European Southern Observatory, Karl-Schwarzschild-Strasse 2, Garching bei Munchen, D-85748, Germany

mid-infrared counterpart points to populations of very hot and small (sub-micron) grains piling up very close to the sublimation radius. For solar-type stars with no known infrared excess, likely to be the most relevant targets for a future exo-Earth direct imaging mission, we find that their median zodi level is lower than 60 (90) zodis with 95% (99%) confidence, if a log-normal zodi luminosity distribution is assumed.

Subject headings: instrumentation: interferometers—infrared: stars—stars: circumstellar matter

1. Introduction

Debris disks found around main sequence stars are the remnants of planetary formation. The outer colder parts of these disks, analogous to our solar system Kuiper-Edgeworth (hereafter Kuiper) belt, were first detected via their mid-infrared (MIR) or far-infrared (FIR) excess emission, and then imaged at visible to sub-millimeter wavelengths. Structures and asymmetries in spatially resolved debris disks have been used to infer the presence of yet unseen planets. The power of this technique was recently demonstrated with the direct imaging of a massive planet at the inner edge of the warped extended dust disk previously detected around β Pic (Lagrange at al. 2009; Macintosh et al. 2014). Conversely, very little is known about the hotter (> 200K) dust component of debris disks, concentrated in the inner few AU of the stellar environment where rocky planets may have formed, similar to the zodiacal dust found in the inner solar system, which originates from the tails of comets and from collisions between asteroids in the asteroid belt.

Indeed, only a few hot debris disks have been found by Spitzer around mature stars from excess emission at wavelengths of 24 μm or shorter (Beichman et al. 2006a; Lawler et al. 2009), and only a few have been unambiguously resolved so far (e.g., Smith et al. (2009)). This observational difficulty results from two main factors: the exozodiacal disks' small angular sizes, and their faintness relative to the host star. Indeed, while cold debris disks cause very significant excesses readily detectable at far-infrared wavelengths, exozodiacal material located in the inner few AU only contributes a small fraction of the stellar MIR flux. In order to reliably detect such tiny ($\simeq 1\%$) excess emission over that expected from the photosphere, direct imaging is required, with the ability to spatially resolve dust from the central star. In the visible, where dust is seen by means of scattered starlight, the contrast required is extremely high and only a space or balloon-borne coronagraph could provide adequate performance. In the infrared, exozodiacal disks produce significant thermal emission and contribute a larger fraction of the stellar flux, making it the spectral range of choice for ground-based exozodiacal studies. With the spatial scales at play, typically 0.1 to a few AU, such direct infrared observations are best accomplished using long baseline interferometry. This was the main goal of the Keck Interferometer Nuller (KIN), a long baseline (85 m) high contrast instrument operating between 8 and 13 μm, especially built to spatially resolve faint structures next to bright stars (Serabyn et al. 2012; Colavita et al. 2013). Exozodiacal observations were carried out with the KIN between 2008 and 2011 through three different Key Science programs (led by Serabyn, Hinz and Kuchner respectively) and one PI program (led by Mennesson). These studies targeted a total of 47 nearby main sequence stars whose basic properties are listed in Table 1. We already analyzed a subset of this sample (Paper I) comprising 23 stars with no previously known dust, and 2 with dust previously detected in the MIR and FIR: η Crv (Beichman et al. 2006b; Chen et al. 2006; Smith et al. 2009) and γ Oph (Su et al. 2008). This initial data analysis was restricted to a single spectral channel spanning 8 - 9 μm, and revealed only one clear excess (around η Crv), and two marginal ones (around γ Oph and Altair). It also provided the best limits to date on 10 μm

exo-zodi levels for a sample of nearby main sequence stars, with a typical measurement uncertainty (1σ) of 150 times the solar zodiacal light emission or 150 "zodis". For all stars in our sample, we define the unit zodi case as a dust cloud with the same optical depth at 1 AU and the same radial density profile as measured in the Solar System (Kelsall et al. 1998), but with an inner dust radius and radial temperature profile that scale with stellar luminosity (see section 3.5 for further details).

In this context, our present goals are to (i) perform a final calibration of the complete KIN sample of 47 stars using a consistent set of rules for data vetting, calibrator diameters and uncertainties, (ii) compute all individual star excess measurements over the full 8 to 13 μm spectral range, divided into 10 spectral channels, (iii) assess possible correlations between basic stellar properties and measured MIR excesses, and (iv) derive conclusions on the prevalence of high levels of exo-zodi emission for nearby Sun-like stars. As the more sensitive Large Binocular Telescope Interferometer (LBTI) exo-zodi survey is just starting, it is also timely to draw a final set of conclusions from the KIN surveys to help refine the LBTI stellar sample selection (Weinberger et al. 2014).

2. Calibration and Data Vetting

The KIN data acquisition principle and reduction technique are fully described in past publications (Colavita et al. 2009; Millan-Gabet et al. 2011; Serabyn et al. 2012) and will not be discussed in detail here. Similar to regular interferometric observations, the correction of instrumental effects is based on interspersed nulling observations of science targets and nearby calibrator stars. These calibrators have well known diameters and are used to derive accurate estimates of the instrumental leakage at the time of science target observations.

2.1. Calibrators

In order to minimize systematic errors in the calibration, calibrator stars were chosen close to the science targets and with similar MIR fluxes. As a result, these calibrator stars were typically giants. In order to most accurately predict their angular diameters, we retained only the observations of giant calibrators with spectral types G, K and early M. We also made a thorough check through the literature and rejected any calibrator with a reference to possible binarity or variability. As stated in Paper I, these different criteria minimize the possibility of infrared emission above photospheric levels [1] (Cohen et al. 1999). The calibrators' limb-darkened (LD) diameters were computed adopting the following set of rules:

- If a calibrator was listed in the Borde et al. (2002) or Merand et al. (2006) catalogs of interferometric calibrators, we adopted its estimated LD diameter, with a relative error bar of ± 5%. This error is conservatively increased in comparison to the catalogs quoted uncertainties (typically 1.5%), reflecting the typical offset measured with respect to long baseline interferometric measurements when available.
- Otherwise we used surface brightness relations, specifically the LD diameter vs (V_0 - K_0) relation, where V_0 and K_0 are the measured V and K magnitudes corrected for interstellar extinction. We

[1] If there was any significant N-band excess emission around the calibrators, this would bias the science target measurements towards lower or even negative null excess levels, which we do not observe.

assumed the extinction to be isotropic, i.e just a function of stellar distance. Because common surface brightness relations are valid over specific ranges of color differences, we then considered two sub-cases:

(i) If the derived V_0 - K_0 was between -0.1 and 3.6, we used the surface brightness relationship established by (Di Benedetto 2005) (equations (2") & (4)). We then applied an LD diameter error bar of ± 6% if the K magnitude came from TMSS (Two Micron Sky Survey IRC catalog Neugebauer & Leighton (1969)) or from JP11 (IRAS catalog, Gezari et al. (1993)) measurements. We used an error bar of ± 10% if the K magnitude came from 2MASS, whose measurements are saturated and fairly inaccurate for our bright calibrators.

(ii) If the derived V_0 - K_0 was between 3.6 and 7 or between -1.1 and -0.1, we used the surface brightness relationship established by Bonneau et al. (2006) (equations 9,10 & table 2 of that paper), in the case of bright objects (V<10, K<5). We applied an error bar of ± 7% if the K magnitude came from TMSS or JP11 measurements. We used an error bar of ± 10% if the K magnitude came from 2MASS.

The error bars quoted above (6, 7 or 10%) were derived by comparing the derived surface brightness LD diameters to those estimated by Borde et al. (2002) and Merand et al. (2006) for an ensemble of 100 calibrators (including those used in this work), assuming that the Borde and Merand values were "the correct ones". It is worth noting that calibrator diameters were estimated in a different way in Paper I, which used Keck Interferometer K-band measurements acquired at the same time as the mid-infrared null measurements. The present calibration strategy leads to slightly revised null values for the 25 science targets already discussed in paper I. However, all changes are within the calibrated null error bars of a few 10^{-3}, to the exception of Altair (see section 5.2).

2.2. Data vetting

For each science target, we only retained null data sequences (or "scans") based on the following criteria: at least one calibrator observation is available within one hour, and the percentage of gated data (Colavita et al. 2009) retained for that scan is greater than 50%, indicating reasonably good phase and angle tracking performance. We also checked that the nightly logsheets reported adequate observing conditions in terms of cloud cover and seeing, no instrumental configuration change or realignment between target and calibrator, no evidence for fast photometry drop outs, and no major issues with the atmospheric dispersion correctors (ADC). Namely, we removed all scans with large sudden jumps or saturation (hard limit reach) of the ADC prisms position, indicating strongly variable or poor instrumental nulls.

3. Results

3.1. Excess Leak Curves

As described in paper I and in Serabyn et al. (2012), the quantity observed by the KIN may be understood by projecting the fringe pattern on the sky: what is measured is the astrophysical flux from the object's surface brightness transmitted through a 4-beam nuller fringe pattern (see Appendix I for a complete description). For the work presented here, we measure and calibrate the transmitted flux (expected to be small) due to dust surrounding the central target stars. Thus, we refer to the basic observable as the flux leakage or simply the "leak". The amount of flux leakage not attributable to the finite size of the central stars is referred to as

"excess leak", and by measuring it we can learn about the amounts of circumstellar dust present. The data reduction steps defined hereafter were applied to all 47 science targets and are identical for all 10 spectral channels covering the full 8 to 13 μm bandwidth of the instrument. Additionally, the real-time archiver saves the signal summed over the two spectral channels between 8 and 9 μm, forming the so-called "8-9 μm null bin" already used in Paper I, which is treated here as an "11-th" channel.

- For each individual stellar scan (typically 5 min long), we computed a raw leak (observed null depth) versus wavelength.

- We then subtracted the instrumental leakage measured on nearby calibrators, which yields the target's calibrated leak versus wavelength.

- Due to their finite extension, all targets observed are slightly resolved by the KIN. In the case of a photosphere represented by a limb darkened disk of diameter $\theta_{\rm LD}$ with a linear limb darkening (LD) coefficient u_λ, the corresponding stellar leak is given by (Absil et al. 2006, 2011):

$$L_{\rm star}(\lambda) = \left(\frac{\pi B \theta_{\rm LD}}{4\lambda}\right)^2 \left(1 - \frac{7u_\lambda}{15}\right) \left(1 - \frac{u_\lambda}{3}\right)^{-1} \quad . \tag{1}$$

  When working in the MIR, LD effects are generally small (< 0.1) for main sequence stars. As a result, we generally assume $u_\lambda = 0$ in the equation above. As long as the linear LD coefficient is smaller than 0.1, this approximation translates into a stellar leak error of a few 10^{-4} at most, which is completely negligible compared to our measurement uncertainty. The only two exceptions are Vega and Altair (see section 5.2). Both are rapid rotators with significant - gravity induced - limb darkening and large enough diameters, and this effect must be taken into account when computing the stellar leak. For Vega, we adopted the model derived by Aufdenberg et al. (2006), which yields $\theta_{\rm LD}= 3.329 \pm 0.03$ mas and $u_\lambda = 0.10$ between 8 and 13 μm. For Altair, we adopted for each KIN observation the position angle (PA) dependent diameter measured by Monnier et al. (2007) with the CHARA interferometer. At each wavelength and for each individual scan, the stellar leak is then subtracted from the calibrated leak defined above, yielding the measured excess leak versus wavelength.

- A single measured excess leak versus wavelength curve is then computed per target, averaging all scans (typically between 1 and 4) obtained under a common set of instrumental conditions, which we refer to as an observational "cluster"[2]. Say that a given cluster (index j) consists of a set of individual scans (index i) characterized at any single wavelength by an excess leak measurement E_{ij} with uncertainty σ_{ij}. The average excess leak E_j corresponding to that cluster is computed as the weighted least squares mean from individual scans

$$E_j = \frac{\sum_i E_{ij}/\sigma_{ij}^2}{\sum_i 1/\sigma_{ij}^2} \quad . \tag{2}$$

- The uncertainty on the cluster excess leak is estimated by computing a statistical "internal" term σ_j^{int}, decreasing with the number of scans but still non-zero if all noisy measurements happen to be equal

[2]Unless a major optical realignment occurred during the observations (e.g., caused by a change of the static delay line position), there is only one observational cluster per night and per target

$$\sigma_j^{int} = \frac{1}{\sqrt{\sum_i 1/\sigma_{ij}^2}} \quad , \tag{3}$$

and a second "external" error σ_j^{ext} which reflects the scatter of individual measurements (weighted standard deviation)

$$\sigma_j^{ext} = \sqrt{\frac{\sum_i (E_{ij} - E_j)^2/\sigma_{ij}^2}{\sum_i 1/\sigma_{ij}^2}} \quad . \tag{4}$$

Both internal and external uncertainties are taken into account and summed in quadrature. The resulting uncertainty is then compared to the systematic error floor σ_{sys} per cluster recommended in Table 2 of Colavita et al. (2009), which is a function of wavelength and stellar flux. Only the larger value is retained and the final leak excess uncertainty per cluster is hence defined as

$$\sigma_j = max(\sqrt{(\sigma_j^{int})^2 + (\sigma_j^{ext})^2}, \sigma_{sys}) \quad . \tag{5}$$

- Finally, in the case where several data clusters are available for a given target, a weighted mean excess leak is computed for each wavelength as

$$E = \frac{\sum_j E_j/\sigma_j^2}{\sum_j 1/\sigma_j^2} \quad , \tag{6}$$

and its uncertainty is estimated as:

$$\sigma = \frac{1}{\sqrt{\sum_j 1/\sigma_j^2}} \quad . \tag{7}$$

As a summary, the final KIN data reduction products consist of stellar excess leak curves measured as a function of wavelength. As described in paper I, in the usual case that the MIR circumstellar (exozodiacal) flux is small compared to the stellar photospheric flux, the excess leak (E) is proportional to the MIR flux emitted by the exozodiacal cloud, expressed as a fraction of the stellar flux. The proportionality factor is the transmission by the sky-projected KIN null fringe pattern, which is discussed in the next section. Thus, for a point source star with no circumstellar material, we would measure E=0, and this fraction increases as more exozodiacal emission is spatially resolved. KIN measured excess leak curves are either accessible per individual scan, per cluster (averaging several scans gathered within a single night), or by averaging data from different clusters/ observing nights, when applicable. Excess leaks were computed for all 47 targets observed. For 44 of them (Fig 1), little or no significant fluctuation is detected between the different scans and all available data are averaged together as described above. The remaining 3 targets are small-separation multiple-star systems exhibiting large null variation vs time as the projected baseline or the companion position varies. In those cases, we show individual scan results (Fig 2) rather than temporal averages. Further details on multiple system observations are given in section 3.3.

3.2. Excess leak versus physical excess

It is important to note that in order to convert a measured excess leak into an actual physical excess, the brightness distribution of the excess source must be known. In particular, because of the interference pattern and the limited field of view of the instrument, the KIN-measured excess leaks are necessarily smaller than the actual astrophysical excesses. A complete description of these effects is given in separate publications (Serabyn et al. 2012; Mennesson et al. 2013), and a reminder of the relationship between measured leak and sky brightness distribution is given in Appendix 1. In particular, any source of circumstellar excess lying (a) inside of the 6 mas KIN inner working angle (IWA), defined as the half transmission point at 10 μm -, or (b) outside of its $\simeq$ 200 mas outer working angle (OWA), set by the instrument 400 mas FWHM field of view, will be strongly attenuated or even completely missed. Using 300 K as a representative temperature of the habitable zone where future exo-Earth imaging missions will concentrate their efforts, and assuming dust emitting like a black-body at thermal equilibrium with the star, we computed the 300 K dust location around all targets. For most stars in the sample (Table 1), the 300 K dust radial distance lies comfortably between the IWA and OWA: any extended dust emission at that temperature (or warmer) will be detected. For such stars, an attenuation factor of $\simeq$ 2 is expected between the measured excess leak and the actual 10 μm excess[3]. For the nearest A and F stars however, the 300 K dust radius lies outside of the KIN field of view, and a significant fraction of the excess may remain undetected by the KIN. This is especially true for Vega, Altair, α Psa, β Leo, β Cas and β UMa, all having hypothetical 300 K (or colder) dust located well outside of the KIN field of view.

3.3. Binary Stars

The KIN geometric field of view radius is limited to 300 mas by a pinhole located in an intermediary focal plane, yielding a FWHM of $\simeq$ 400 mas when taking propagation, diffraction and scattering effects into account (Colavita et al. 2013). Assuming an equal brightness binary system, we find that any companion located $>$ 5 arcseconds away will have negligible impact on the KIN signal and can be safely ignored in the data processing. Using the Washington Visual Double Star Catalog (Mason et al. 2001) and the Sixth Catalog of Orbits of Visual and Binary Stars (Hartkopf et al. 2001), we find however that nine of the 47 target stars had stellar companions within 5" at the time of the observations. The presence of these nearby companions affects data analysis at different levels depending on individual systems characteristics:

- Both χ^1 Ori and τ Boo have stellar companions within 5", but with no effect expected (nor detected) on the measured leak. These 2 sources are indicated as type "bin 1" in Table 1. χ^1 Ori is a single-line spectroscopic and astrometric binary with a faint companion ($\simeq$ 1.5% flux ratio at H-band, Koenig et al. (2002)) located 700 mas away at the time of the KIN observations (Hartkopf et al. 2001). Adopting the effective temperatures derived for the 2 components (5920 K and 3200 K) and assuming blackbody stellar emission, the flux ratio is still only 3% at 10 microns. This means that the companion contributes negligible flux inside the field of view compared to the $\simeq$ 0.2% KIN measurement uncertainty level. The astrometric companion to τ Boo has been directly imaged in 2001 at a separation of 2.7" with a relative flux of 1% at 800 nm (Roberts et al. 2011), corresponding to $\simeq$ 4% at N-band when adopting

[3]This factor corresponds to the average transmission value over the region extending from the IWA to the OWA.

the F6IV / M2V spectral types of Hale (1994) and assuming blackbody stellar emission. The separation predicted at the time of the KIN observations is 1.6" (Hartkopf et al. 2001), still far enough that no significant contribution to the null signal is expected from this faint companion. As far as the KIN measurements are concerned, these two stars are then effectively single, bringing up the total of KIN "single" stars to 40.

- For ι Peg, the companion is well inside the KIN field of view, but we found no obvious signature from a resolved companion in the leak excess curves, i.e., no variations with time or projected baseline. However, the companion is relatively bright, with a flux ratio of 4:1 at N band and may impact the measured null depth. We used the orbit and stellar system parameters of Boden et al. (1999) to determine the companion location at the two epochs of the observations, and found separations of 2.38 and 2.54 mas, i.e., significantly smaller than the spatial resolution of the nuller. Computing the leak expected from this binary system, we found that the companion caused an extra leakage of 8 x 10^{-4} at 8 μm and even less at longer wavelengths. ι Peg's excess leak curve shown in Figure 1 has been corrected for this small effect ("bin 2" object type in Table 1).

- For 61 Cyg A, δ Tri and β Tri, no obvious signature was found either in the measured leak excess curves, versus time or wavelength. We used published orbits from the Sixth Catalog of Orbits of Visual and Binary Stars (Hartkopf et al. 2001) to compute the companion locations at the epochs of the KIN observations. These companions are all well inside the KIN field of view (and located in the "positive leakage" area, see Appendix 1 and Figure 11). However, and unlike the case of ι Peg, we have found no information from which the components flux ratio could be derived ("bin 3" object type in Table 1). Therefore, we perform no additional correction to account for the presence of a known companion in these systems. Subtracting the companion's contribution to the leak would only reduce the inferred leak excess and corresponding exozodiacal level, and thus any results derived for these stars, whether the excess leaks shown in Figure 1 or the zodi levels listed in Table 2, are to be interpreted as upper limits .

- HD 83808, α Crb and β Per (the triple system Algol) have clear signatures of companions in the excess leaks measured (Figure 2), showing very large fluctuations versus hour angle, between 4 and 15% peak to peak. Given the uncertainties in the nuller off-axis transmission values and binary system parameters (companion position, diameter and relative flux), the effect of these companions can not be removed with high precision. As a result, these three stars are discarded from any further derivation of circumstellar dust excess and exo-zodi level ("bin 4" object type in Table 1).

The effective KIN exozodi sample is then reduced to 44 stars: 40 effectively single for KIN, one binary system with accurate dust excess determination (ι Peg), and three more binary systems for which only upper limits are derived (61 Cyg A, δ Tri and β Tri).

3.4. 8 to 9 μm excesses

As can be seen in all panels of Figure 1, the excess measurement uncertainty increases sharply with wavelength across the bandpass. The reason is that various instrumental factors (finite diffraction effects, material absorption, and pinhole mode matching), and the increased thermal background strongly reduce the KIN

spectral sensitivity toward the red end of the bandpass. In addition, atmospheric dispersion is actively corrected around 9 μm, yielding larger chromatic effects and null uncertainties at longer wavelengths (Colavita et al. 2009). Under these conditions, the most reliable excess estimates come from measurements obtained in the 8 to 9 μm bin. The quantity of interest is the ratio of the measured leak excess to its uncertainty, which we refer to hereafter as the "excess significance". It is worth noting that due to instrumental noise, the measured leak excess can be negative, and the excess significance as well. All excess measurements are summarized in Table 2 and show that five stars have an 8 to 9 μm excess leak with a significance larger than 3 σ. Among them, only η Crv shows a large (8σ) excess. The other four are β UMa, β Leo, ζ Lep and γ Oph, all showing excesses at the 3 to 4 σ level. While 8 to 9 μm excesses around η Crv and γ Oph were already reported in Paper I, KIN excesses around the other three stars are reported here for the first time. Noticeably, all five stars had FIR excesses previously reported. A more detailed analysis of these five stars is given in section 5.1, including their full 8 to 13 μm measurements.

3.5. Zodi levels

In order to interpret the excess measurements and compare them to the Solar System case, we used the Zodipic code (http://ssc.spitzer.caltech.edu/dataanalysistools/ tools/contributed/general/zodipic/) to create images of zodi clouds around each target. Zodipic synthesizes brightness distributions of exozodiacal clouds based on the empirical fits to the observations of the solar zodiacal cloud made by COBE (Kelsall et al. 1998). When Zodipic generates a model brightness distribution for a zodi disk analog around a star other than the Sun, the dust has the same optical depth at 1 AU and the same radial density profile as in the Solar System. As a convenient unit, we refer to this model as corresponding to 1 "zodi". Zodipic scales the radial temperature profile with stellar luminosity, and the inner dust radius is set by a dust sublimation temperature of 1500 K. The dust inner radius is thus dependent on stellar spectral type, and ranges from 0.004 AU for the coolest star in our sample (the M2V star HIP 54035) to 0.18 AU for Vega. In the Zodipic code, the dust density can be treated as a free parameter, allowing generation of brightness distributions for scaled version of the Solar System (the total flux due to the circumstellar dust scales linearly with zodi level). Since the 8 to 9 μm KIN measurements are of higher quality, we restricted the zodi-level calculations to that spectral bin, which also ensures continuity with the results derived in Paper I. In order to convert the measured 8 to 9 μm excess leaks to number of zodis, we used the procedure described in section 4.2 of Paper I, summarized below. A 1 zodi dust cloud image (not including the central star) is generated around each star considered using the zodipic model, and the overall dust flux transmitted through the instantaneous (8.5 μm) KIN transmission pattern (see Appendix 1) is computed. The resulting flux is then divided by the 8.5 μm stellar flux, yielding the leak excess expected for a 1 zodi exozodical dust cloud, and a final estimate of the zodi level required to match the observed excess leak. Since the dust cloud inclination and phase angle are generally unknown (except in a few cases, see section 5.1), this operation is repeated for different exozodiacal disk orientations, from face-on to edge-on, with position angle parallel and perpendicular[4] to the instantaneous direction of the long baseline fringes. These orientation effects are small compared to the KIN excess measurement error bars, but are included in all derived zodi levels and uncertainties, which are listed in Table 2. We note that although unphysical, negative zodis are allowed as a result of the error

[4]Because of the finite scale height of the zodi dust cloud and the high spatial resolution of the KIN, an edge on-disk still contributes a significant null excess whatever the baseline orientation.

bars on the leak measurements. This procedure is exactly the same as used in Paper I (section 4.2). We note however that in this paper we have used more accurate estimates of the stellar flux in the KIN 8-9 μm spectral bin. We have used Akari fluxes in the 9 μm band, color corrected, and scaled to the 8.5 um KIN effective wavelength using a Rayleigh-Jeans assumption. These revised stellar fluxes result in new estimates of the zodi levels for the 25 stars of Paper I, in average 40% higher, and supersede those of Paper I.

3.6. 8 to 13 μm excesses

In addition to the 8 to 9 μm bin, we made use of the measurements obtained over the full N-band, with the goal of identifying possible new excess stars, i.e., stars with excess only present at the longest KIN wavelengths. To this end, we interpreted each of the 10 spectral channel excess leaks as individual measurements of a constant broad-band 8 to 13 μm excess and formed an average. A difficulty in averaging such measurements is that some correlation is suspected between the different KIN spectral channels (Colavita et al. 2009), but that the actual spectral data covariance matrix is unknown. In this case where the exact correlation pattern is unknown, a robust way of estimating the mean is to ignore all correlation terms and use a simple weighted average (Schmelling 1995). Assuming that each spectral channel (index k) is characterized by a measured excess leak E_k with 1σ gaussian error σ_k, we then estimated the broad-band excess as:

$$E_{8-13} = \frac{\sum_k E_k/\sigma_k^2}{\sum_k 1/\sigma_k^2} \tag{8}$$

The uncertainty on this estimated broad-band excess is more difficult to assess. In order to bound the problem, and since correlation factors are unknown, we examine two extreme cases.

3.6.1. Uncorrelated spectral channels

If all spectral channel measurements were completely uncorrelated (the most optimistic scenario), the uncertainty on the broad-band excess would be:

$$\sigma_{8-13} = \sqrt{\frac{1}{\sum_k 1/\sigma_k^2}} \tag{9}$$

In this uncorrelated case, the broad-band excess significance would then be given by:

$$S_{uncor} = \frac{E_{8-13}}{\sigma_{8-13}} = \frac{\sum_k E_k/\sigma_k^2}{\sqrt{\sum_k 1/\sigma_k^2}} \tag{10}$$

In particular, if all 10 spectral channels had the same measurement uncertainty $\sigma_k = \sigma_0$ (a simple illustrative case to consider), one would get:

$$\begin{aligned} E_{8-13} &= < E_k > \\ \sigma_{8-13} &= \frac{\sigma_0}{\sqrt{10}} \\ S_{uncor} &= \sqrt{10}.\frac{< E_k >}{\sigma_0} \end{aligned} \tag{11}$$

The broad-band excess derived is simply the mean of observed values, and its significance increases as the square root of the number of spectral channels, as expected for uncorrelated data.

3.6.2. Fully correlated spectral channels

Unfortunately, excess measurements obtained in different spectral channels are known to be partially correlated (Colavita et al. 2009), an effect believed to be caused by residual thermal background correlation at the single telescope cross-combiner level, and by small differential dispersion effects between science targets and calibrators. In order to derive the most conservative error bar on the broad-band excess, we assume here that the various spectral channels measurements are fully correlated (worse case scenario). In that case, the uncertainty on the broad-band excess is given by:

$$\sigma_{8-13} = \frac{\sum_k 1/\sigma_k}{\sum_k 1/\sigma_k^2} \tag{12}$$

and the broad-band excess significance becomes:

$$S_{cor} = \frac{E_{8-13}}{\sigma_{8-13}} = \frac{\sum_k E_k/\sigma_k^2}{\sum_k 1/\sigma_k} \tag{13}$$

And if all 10 spectral channels had the same measurement uncertainty $\sigma_k = \sigma_0$, one would now get:

$$\begin{aligned} E_{8-13} &= < E_k > \\ \sigma_{8-13} &= \sigma_0 \\ S_{cor} &= \frac{< E_k >}{\sigma_0} \end{aligned} \tag{14}$$

Compared to the uncorrelated case above, the uncertainty is now higher by $\sqrt{10}$, and the broad-band excess significance is reduced by this factor. Table 2 summarizes the broad-band 8 to 13 μm excess leak measured for each star, with the uncertainties and significances derived in both the uncorrelated and fully correlated cases. The former is only given for reference (best case scenario). Only the values derived in the fully correlated case (worse case scenario) are considered for determining a potential 8 to 13 micron excess and for further statistical analysis.

3.6.3. 8 to 13 μm excess stars

Based on the results of Table 2, and assuming all spectral channels measurements are fully correlated, only two stars show a broad-band excess with a significance larger than 3σ: η CrV and ζ Lep. However, the

statistical analysis conducted in the next section suggests that many more stars have a broad-band excess, albeit close to the detection limit of the KIN.

4. Statistical Analyses

Rather than looking at the results for individual stars, we use here the whole sample or specific sub-groups of it. The goal is to obtain more sensitive estimates of the number of stars with a MIR excess and look for possible statistical trends, such as correlation of the observed KIN excesses with basic stellar properties. In order to avoid any possible contamination of the null measurements, all further analyses are limited to the 40 "effectively single" stars, as defined in Section 3.3.

4.1. 8 to 9 μm excess distribution

Figure 3 (panel A) shows the histogram of excess significance measured in the 8 to 9 μm bin. As already discussed in section 3.3., five stars show an excess significance greater than 3 and have hence a formally detected KIN excess. But as can be readily seen, the observed distribution tells more: it is highly non symmetrical and shows a tail towards larger excesses. Excess measurements with a "negative significance" are a consequence of the measurement noise; but this also means that such data can be used to infer the instrumental noise distribution. The dotted line shows the best gaussian fit to these negative significance histogram data (after symmetrizing around x=0 and taking into account the averaging due to finite bin size). The best fit gaussian noise distribution has a standard deviation of 1.002, very close to unity, as would be expected from the empirical standard deviation of many independent realizations of the variable $(E_{8-9}/\sigma_{E_{8-9}})$. Further evidence for the validity of this instrumental noise estimation and its gaussianity is given in section 4.5.[5] Although they can not be formally identified as bona fide excess stars, there are several more targets with excess significance at the 1σ to 3σ level than predicted by instrumental noise only: in addition to the five stars with significant excess, about 10 more stars lie close to the KIN detection limit and would be interesting targets for an instrument providing better contrast, even by just a factor of $\simeq 3$.

4.2. Exo-zodi level distribution

Figure 3 (panel B) shows the histogram of zodi levels derived around the 40 stars in the sample. Here again, the dotted line shows the best fit gaussian to the negative measurements, providing an estimate of the measurement noise distribution. Its standard deviation is 190 zodis, a value very close to the mean and median zodi measurement uncertainty of the overall sample (202 and 188 zodis respectively). The zodi level and the excess significance are not necessarily related, since zodi level and uncertainty levels are a priori uncorrelated (e.g., a large zodi level might be associated with a large uncertainty and hence a low detection confidence level.) This means that the excess significance and zodi level histograms provide independent information, at least to some extent. However, and quite interestingly, a similar behavior is found in the

[5]As shown in the top left panel (A) of Figure 4, which concentrates exclusively on the 20 stars with no infrared excess previously known, a zero mean gaussian distribution with a standard deviation close to unity is also found to be a very good fit to the data (also see Paper I).

empirical histograms of both quantities. Once again, there seem to be significantly more than five stars with zodi levels higher than what the noise distribution predicts. This excess is particularly visible between 150 and 450 zodis.

4.3. Broad-band excess distribution

Figure 3 (panel C) shows the histogram of excess significance measured between 8 and 13 μm, assuming that all spectral channels are fully correlated. This assumption yields the lowest possible excess significance levels given the data, and hence the most conservative estimates of broad-band excess detection. While only 2 stars (η Crv and ζ Lep) show formally detected correlated broad-band excesses with a significance greater than $3\,\sigma$, the observed distribution is again very asymmetric, and the number of stars with significance between 1σ and $3\,\sigma$ again exceeds the levels predicted by pure instrumental noise. In addition, the best fit noise distribution (dotted curve) derived from "negative excess" data has a standard deviation of 0.68. This low value suggests that the broad-band excess significance estimates are generally underestimated by a factor of $\simeq 1.5$. In other words, any star with a correlated broad-band excess quoted at the 2σ level is more likely a 3σ excess. Some further evidence for overestimated error bars comes from the analysis of the sub-sample of 20 stars with no infrared excess previously known, presented in section 4.5. [6] Applying a $2\,\sigma$ cut instead of $3\,\sigma$ (per the argument presented above) leaves 8 sources: the five stars with 8 to 9 μm excess already listed in section 3.3 (η Crv, β UMa, β Leo, ζ Lep and γ Oph), along with Fomalhaut (α Psa), Altair and Vega.

4.4. Influence of Spectral Type and Age

Considering the 8 to 9 μm excess significance measured as a function of spectral type, KIN excesses at the $3\,\sigma$ level or higher are exclusively found around early type stars. With the exception of η Crv (F2V type), all stars showing an 8 to 9 μm excess are A stars. Of course, the analysis suffers from small number statistics, but the observed fractions of excess stars are very different at 4/11, 1/13, 0/9 and 0/7 for A, F, G and K/M[7] stars respectively. Extending the analysis to the KIN broad-band 8 to 13 μm measurements, A stars are even more favored: among the 8 stars showing an excess significance at the $2\,\sigma$ level or higher, 7 are A stars. This is in contrast with the results found for stars with no previously known infrared excess (Paper I, Appendix A), for which no correlation was found between excess leakage and stellar effective temperature. In fact, if any instrumental bias was affecting the measurements, it would rather tend to underestimate excesses around nearby A and early F stars. Indeed, while the KIN baseline is long enough to comfortably resolve the inner zodi regions of even the coldest and most distant stars in the sample, only nearby A and F stars have 300 K dust radii lying outside of the KIN OWA (Table 1). As discussed before (section 3.2), this effect is precisely the strongest around Vega, Altair, α Psa, β Leo and β UMa. This suggests that the small excess leak detected around some of these stars could actually trace a significantly larger mid-infrared

[6] In this case, a zero mean gaussian distribution with a standard deviation of 0.64 - again notably smaller than unity - is found to be the best fit to the broad-band excess significance histogram (Figure 4, top right panel C).

[7] There was only one M star in the sample (HIP 54035, M2V spectral type). It was grouped with the 6 K stars for the purpose of this analysis.

physical excess (see section 5.2 for discussion of individual targets). The higher occurrence of 10 μm excess observed around A stars appears then to be a real astrophysical trend. Since A stars have the shortest main sequence lifetime, this apparent correlation of the KIN excess with spectral type could also be caused by a correlation with age. A similar trend was observed at far and near infrared wavelengths (Trilling et al. 2008; Absil et al. 2013).

4.5. Connection with excesses detected at other IR wavelengths

As summarized in Table 2 (last column), 20 of the KIN "single" stars have either a "cold" FIR (> 60 μm) excess or a "hot" NIR ($\simeq 2.2$ μm) excess detected. While the former excess type is likely due to outer dust and comet reservoirs analogous to the solar system Kuiper belt, the origin of the NIR excess is still poorly understood. The most likely explanation is the presence of submicron sized hot dust particles piling up close to the sublimation radius of these stars (Absil et al. 2013; Mennesson et al. 2011; Lebreton et al. 2013). In order to help understand the origin of those various types of infrared excess, we correlated them with the detected KIN excess.

Figure 4 compares the distribution measured for stars with no previously known infrared excess (Group 1), to that obtained for stars with either a cold or a hot infrared excess previously reported (Group 2). Each group contains 20 stars each, allowing a straightforward comparison of the observed distributions. While distributions measured for the first group are centered around zero and fairly symmetric, the second group distributions are heavily skewed towards positive detections. This effect is especially pronounced for the broad-band KIN measurements (Figure 4, panels C & F). Indeed, while none of the 20 stars in Group 1 show a large broad-band excess significance, - all below a value of 1.7 -, eight of the Group 2 stars show a broad-band excess significance larger than 2. A similar effect is seen between the zodi level distributions of the two groups (Figure 4, panels B & E): stars in Group 2 have their observed distribution shifted towards higher zodi levels, exhibiting significantly more stars in the 200 to 400 zodi level bin and at zodi levels above 600 zodis. Even after excluding η Crv and its unusually bright MIR dust emission, the weighted mean of the zodi levels measured for Group 2 stars is 206 zodis, significantly higher than the value measured for Group 1 stars, which is 15 zodis. The distributions measured for the two groups of stars are then significantly different, pointing to a positive correlation between the measured KIN MIR excess and the presence of a previously known infrared excess. In fact, and as shown in Table 3, most of these infrared excess stars (16 out of 20) have a FIR excess, and it is thus really the presence of a cold FIR excess which is the strongest indicator of a MIR excess. Out of the 16 stars with a known FIR excess, 5 show a KIN excess. In comparison, of the 24 stars that have no cold excess, none show a KIN excess. A Fisher's exact test shows that there is only a 0.7% chance of detecting rates as discrepant if the two groups had the same distribution. This apparent correlation of warm (zodi-like) and cold (Kuiper-like) infrared excesses is explored more quantitatively in section 4.6.

Figure 5 further examines the possible correlation of the KIN measurements with specific types of infrared excess (or lack of it). It shows the KIN excess rates derived for 6 different sub-groups from the original sample: stars with previously known excesses (cold or hot, 20 of them), cold excess (16), cold excess only (9), hot excess (11), hot excess only (4), and stars with no infrared excess reported (20). For each sub-group, the KIN excess rate in the 8 to 9 μm bin is defined as the fraction of stars showing an excess significance larger than $3\,\sigma$. For the sake of this analysis, the KIN excess rate in the 8 to 13 μm region is defined as the fraction

of stars showing a correlated excess significance greater than $2\,\sigma$, which includes 6 bona fide excess stars and 2 KIN excess candidates (Altair and Vega, see section 5.2). The (asymmetric) statistical uncertainty on the excess rate results from a numerical integration of the binomial distribution. As described in the appendix of Burgasser et al. (2003), the excess rate lower and upper uncertainty limits are computed so that the integrated probability to fall between these limits is 68.2% (34.1% on each side of the observed excess rate), equivalent to the confidence level of $\pm$ 1 σ Gaussian limits. The largest KIN excess fraction is found around stars with a previously known cold excess: between 5/16 and 7/16 depending on the wavelength range and detection threshold used. In comparison, a smaller fraction of stars with a hot excess show a MIR excess: between 1/11 and 4/11, depending on the wavelength range and detection threshold used. However, most of these hot excess stars have a known cold excess as well. Restricting to stars with a "hot excess only" leaves 4 stars, and none of them show an excess, to the possible exception of Altair, which shows a candidate KIN excess (see section 5.2.3).

4.6. Underlying zodi luminosity distribution

Given the observed distributions, we attempt here to derive some relevant information about the "true" underlying zodi luminosity distribution of main sequence stars. There are several difficulties to overcome in order to do so, including possible biases in the sample, finite sampling errors, and measurement noise. We address here these different issues and present the final constraints that can be derived from the KIN measurements.

4.6.1. Sub-groups of stars

In order to reduce biases in the overall sample, while still keeping a statistically significant number of stars, we first split it into the two groups defined above and studied the characteristics of each group independently. Group 1 is composed of 20 targets with no previously reported infrared excess of any kind. It contains no A stars, and can be essentially seen as a sample of solar type stars (9 F, 6 G, 4 K, 1 M). It is the relevant group to characterize in preparation for a future exo-Earth direct imaging mission around sun-like stars[8]. Conversely, Group 2 corresponds to targets with previously reported infrared excesses (mostly cold ones), and is composed of A stars in majority (11 A, 4 F, 3 G and 2 K). Since η Crv is a clear outlier, and a very rare case ($\simeq$ 1 in 10^4 according to Kennedy & Wyatt (2013)) of a $>$ 1 Gyr old F star with a large N-band excess, we removed it from all further sub-groups analyses. While interesting to study for comparison, Group 2 is admittedly more heterogeneous than Group 1, and we further divided it into two more uniform subgroups: Group 2a, composed of 15 stars with a FIR (cold) excess, and Group 2b, which is further restricted to the 8 solar type (FGK) stars with a FIR excess. Comparing the properties of Groups 1, 2a & 2b should help further assess whether the existence of a cold dust reservoir is a key factor, regardless of spectral type.

[8]Especially that such a mission will likely avoid any rare solar type star with a previously known bright FIR excess.

4.6.2. Maximum Likelihood estimations of the underlying zodi luminosity function

One simple way to analyze the data is to assume some representative underlying zodi distributions which are fully characterized by one or two parameters. We tested three kinds of distributions: uniform, truncated gaussian and log-normal, and estimated their parameters (denoted $\vec{\theta}$) using a maximum likelihood estimation method (MLE). More precisely, if the assumed zodi luminosity function is $p(z)$, and each star group contains a set of N independent identically distributed observations $(z_i,\, \sigma_i)_{1\leq i\leq N}$, the likelihood estimator of parameters $\vec{\theta}$ given the data is computed as:

$$L(z_1, z_2, ..., z_N | \, \vec{\theta}) = \prod_{i=1}^{N} p_{noisy}(z_i, \vec{\theta}) \tag{15}$$

with

$$p_{noisy}(z_i, \vec{\theta}) = [p(z) * gaussian(0, \sigma_i)]_{(z_i)} \tag{16}$$

and where the $*$ sign designs a convolution operation. Indeed, for each star, the observed zodi value is affected by a random measurement error, represented by a zero mean gaussian noise with known standard deviation σ_i, and this corresponds to a convolution operation in distribution space. For each zodi distribution assumed, the distribution parameters are determined by maximizing the likelihood estimator of equation 15. In order to estimate confidence intervals on these parameters, we use regular maximum likelihood estimators properties described in Appendix 2. For correct interpretation of these MLE results, it is important to recognize that while the MLE distribution fits the data best, a range of distributions are also compatible with the data, and this uncertainty is captured in the distribution parameter(s) likelihood curves.

Figure 6 shows the results obtained when assuming a uniform zodi level distribution extending from 0 to some maximum value Z_{max}, the only distribution parameter in this simple case. The upper panels show the likelihood curves and maximum likelihood parameters derived for the 4 different groups of stars considered. The parameter 68%, 90% and 98% confidence intervals (respectively 84%, 95% and 99% for one-sided lower or upper bounds) are indicated by the intersection of the likelihood curves with the three corresponding horizontal lines. The maximum likelihood distribution and resulting fraction of stars above a given zodi level are shown in the middle and lower panels of Figure 6. In the uniform zodi model case, the maximum likelihood zodi distribution is significantly narrower for stars with no previously known excess (Group 1) than for any other group, and this result still holds when taking distribution estimation uncertainties into account. At the 99% confidence level, the median zodi value ($Z_{max}/2$) is below 75 zodis for Group 1 stars, while it is above 130 zodis for stars with a cold excess (Group 2a) and above 85 zodis for FGK stars with a cold excess (Group 2b). Because Group 2b contains only 8 stars, its zodi distribution extent and parameters are generally not as accurately constrained as for the other groups, which can be readily seen in the likelihood curves.

Figure 7 and Figure 8 show the results of similar analyses conducted assuming more realistic zodi luminosity functions: a truncated (positive) gaussian and a log-normal zodi distribution, respectively. Both types of distributions provide very similar results with the data MLE analysis: the zodi distribution of Group 1 stars is found to have the smallest extent, peaking towards the lowest zodi values, while fairly identical quasi-gaussian distributions are found for stars in Groups 2 & 2a, centered around a level of 200 zodis (consistent with the findings of section 4.2). Group 2b mean zodi levels are less accurately constrained, but are found fairly similar to those of Groups 2 & 2a, although the distribution derived for Group 2b appears wider, with

a larger fraction of stars at low zodi levels.

The overall results of these maximum likelihood analyses are summarized in Table 4, which indicates the median zodi values derived for each group and for the different types of distributions assumed. For solar type stars with no excess previously detected, the derived maximum likelihood median values are consistently below 20 zodis. In the case where the underlying distribution is represented by a log-normal distribution, we further find that the median zodi level for this group is lower than 60 solar zodis with 95% confidence, and lower than 90 solar zodis with 99% confidence. For stars with a known reservoir of distant cold dust (Group 2a), we find a most likely median zodi level of about 200 zodis, and above 140 zodis with 95% confidence. This is a factor of a few below the detection limit of the instrument, but still significantly higher than for Group 1 stars. There is then a statistically significant correlation between the existence of a cold FIR excess and the strength of the 10 μm excess. Interestingly, this correlation still holds when excluding A stars and only keeping solar type stars (Group 2b), in which case the median zodi value is still above 60 solar zodis with 95% confidence. Another interesting feature is that even when taking into account the uncertainty on the derived distribution parameters, many of the stars with a cold excess apparently have MIR excesses clustering between $\simeq$ 100 and $\simeq$ 400 solar zodis, right below the detection limit of the instrument.

4.6.3. Estimating the "N-sample" zodi luminosity function

Finally, we explored the possibility that the underlying zodi luminosity distribution might be estimated "blindly", i.e., without any a priori assumption on its shape. For each group of stars considered, there are N zodi level measurements and associated uncertainties (Table 2) referred hereafter as $(z_i,\ \sigma_i)_{1\leq i\leq N}$. Given these observations, assuming that the measurement noise is a zero mean gaussian and using Monte-Carlo simulations, it is possible to estimate the zodi luminosity function of the N-sample. The approach we used to do so is based on an iterative blind deconvolution method (Mennesson in prep). As a first iteration, we consider a uniform distribution ranging from 0 to some maximum zodi level larger than any of the observed values (say 10000 solar zodis). We denote by $p_1(z)$ this initial guess distribution, and by $P_1(z)$ the corresponding fraction of stars with zodi levels above a certain level z. A large number (e.g., $N_{mc} = 10^6$) of zodi values are then randomly drawn from it, and for each star observed with measurement uncertainty σ_i, N_{mc} "measured" zodi values are simulated. Among the values falling within a small interval centered around z_i, only a fraction have nominal (no noise) zodi values larger than z. Denoting this fraction $P_2(z|z_i)$, repeating and averaging over the N stars yields $P_2(z)=\sum_{i=1}^{N} P_2(z|z_i)/N$, the second iteration (and better) estimate of the underlying cumulative zodi level distribution given the data. Iterating on this procedure converges to a final estimate of the N-sample zodi luminosity function and its cumulative fraction, as represented in Figure 9 for each of the 4 groups of KIN targets. While the 4 distributions found are very dissimilar and likely reflect some real physical differences between the different groups, the best that can be retrieved using this procedure is the luminosity function of the N-sample, and it remains challenging to draw from it any quantitative information about the underlying (infinite sample) zodi distribution, for the reasons detailed in the next section.

4.6.4. Finite sampling and measurement uncertainties

Finite sampling effects are well understood and described by Bernoulli statistics. Let us assume that the underlying (infinite) population has a cumulated probability $P(z)$ that a star zodi level be above an arbitrary threshold value z. If N stars are randomly drawn from that stellar population and perfect (noiseless) measurements are made of their zodi levels, the empirical fraction $P_N(z)$ of this N-sample provides an unbiased estimate of $P(z)$ (i.e., converging towards it for large values of N), with a $1\,\sigma$ spread equal to $\sqrt{P*(1-P)/N}$. This shows in particular that the largest measurement uncertainty is found for $P = 0.5$, which corresponds to the median zodi value of the distribution. For $N = 20$ for instance, this means that even with a perfect instrument, $P(z)$ can not be measured with a $1\,\sigma$ uncertainty lower than 11.2% at the median zodi level of the distribution, whatever its value is [9]. It also shows that the $1\,\sigma$ offset between the N-sample distribution and the true distribution depends on the distribution itself (via $P(z)$). In other words, even for perfect measurements, the retrieved N-sample distribution of Figure 9 generally differs from the true distribution, and the offset between the two, which sets the estimation uncertainty, is difficult to quantify.

Additionally, the observed zodi levels are affected by the KIN measurement error, which is 200 zodis per star in average, meaning that the N-sample distribution itself is not perfectly measured. Numerical simulations - and common sense- show that if N is the number of measurements, then no information can be reliably retrieved over zodi intervals much smaller than $\simeq 200/\sqrt{N}$. It also means that if the underlying distribution is significantly narrower than this limit, its actual shape can not be derived accurately by a blind method. We verified this numerically by randomly drawing N zodi levels from a"perfectly known" exozodiacal luminosity distribution, adding gaussian measurement noise with a 1σ error of 200 zodis and applying the blind deconvolution method described above to the resulting set of observed values. The algorithm converged to a single solution in all cases simulated, but only provided correct (unbiased) estimates of the drawn distribution when the parent distribution was broader than $\simeq 200/\sqrt{N}$, which corresponds to a width of about 50 zodis in the case of 20 stars. In order to derive information on the shape of such a narrow distribution, some a priori assumption must be made on the nature of the distribution (e.g. gaussian or log-normal) so that only one or two ensemble parameters need to be derived down to the $\simeq 50$ zodi accuracy level (e.g., the mean or median). For zodi luminosity distributions derived using the blind deconvolution method (Figure 9), we used a bin size of 25 zodis. This value provides adequate sampling given the smallest structures that can be reasonably identified given our measurement uncertainties.

4.6.5. Summary of zodi level distribution modeling results

Because of the finite sampling and measurement uncertainty effects described in the previous section, we regard the results of the blind deconvolution method as more qualitative than the MLE results, especially for solar type stars with no previous excess (Group 1), which seem to exhibit a narrow distribution skewed toward low zodi values. For such stars, we favor the results obtained assuming a truncated gaussian (Figure 7) or a log-normal (Figure 8) distribution, which are summarized in Table 4. We note however that many of the distributions characteristics derived by the blind deconvolution method are consistent with the results found

[9]Conversely, as the value of P gets close to 0 or 1, the uncertainty diminishes, although the actual distribution of measured values becomes highly skewed and the $1\,\sigma$ spread is no longer a good metric to use for error bars.

using the maximum likelihood estimations in the log-normal and truncated gaussian cases. For Groups 2 & 2a, the derived zodi distributions are similar and show a large fraction of stars with zodi levels around 200 to 300 zodis. Since the blind deconvolution method does not assume any simple a priori shape, its derived distributions present additional complex features. A compelling one is the double peak distribution found for Group 2b (Figure 9), which suggests that solar stars with FIR excess previously detected can also have low levels of MIR zodi emission. In other words, while all stars with a detected KIN MIR emission have a large cold FIR excess, the reciprocal may not be true. The tail found at low zodi values for Group 2 stars may also be real, and is much attenuated for Group 2a stars. This reflects the fact that stars with a hot excess but no cold excess (only present in Group 2) have statistically lower zodi levels than those with cold excess detected. This difference between the distributions derived for Groups 2 & 2a at low zodi levels is also seen in Figure 7 and Figure 8.

4.7. Discussion

4.7.1. Warm exo-zodi dust and cold outer dust reservoir

While there is strong apparent correlation of the KIN results with spectral type (and possibly age), because no main sequence star later than F2 shows a mid-infrared excess, another key parameter is then the presence of cold dust in the system. From the sample of 40 stars surveyed, it appears that if a star has a cold FIR excess, it has a higher probability of showing a 10μm excess strong enough to be detected by the KIN. Reciprocally, and may be more interestingly, all five stars with a formally identified KIN excess had a previously known far infrared excess attributed to a cold reservoir of dust and cometary material. In other words, large amounts of distant cold dust seem to be required for there to be much warmer exo-zodi emission detectable by the KIN around 10 μm, which necessarily originates from within the first few AUs. The statistical analysis presented in the previous section further establishes and quantifies this connection. It shows that over a wide range of reasonable assumptions for the shape of the underlying zodi luminosity function, stars with a cold excess (regardless of spectral type) have a median zodi value *above* $\simeq$ 140 zodis with 95% confidence. This is in stark contrast to the case of stars with no cold dust reservoir, for which the median zodi level is found *below* 60 zodis with 95% confidence under the same assumptions. As shown in section 4.6 and Table 4, the correlation between warm (zodi-like) and cold (Kuiper-like) dust is also observed when concentrating on solar-type stars: FGK stars with a cold excess (Group 2b) have a statistically larger exo-zodi level than those with no cold excess (Group 1). Although this particular result would benefit from observations of a larger sample, such stars are then a priori bad targets for future direct imaging missions searching for Earth-like planets around Sun-like stars. While warm dust detected by the KIN necessarily resides within a few AU from the host star, its correlation with the presence of cold dust suggests that it finds its origin in the outer regions of the system. This is in contrast to an "in-situ" scenario where warm dust would be formed locally by collisions of parent bodies located in the inner few AUs, in which case only a MIR excess is detected, as observed around very few main sequence solar-type stars, such as HD69830 (Beichman et al. 2005, 2006b), BD+20307 (Weinberger et al. 2011) and HD 15407A (Fujiwara et al. 2012). A popular mechanism for feeding dust to the inner system is the steady state cometary delivery scenario (e.g., Wyatt et al. (2007); Bonsor et al. (2014)). In that case, dust and cometary material from a more distant planetesimal belt is being scattered inward because of dynamical perturbations (Nesvorny et al. 2010; Bonsor et al. 2012; Bonsor & Wyatt 2012). This would resemble the "falling evaporating bodies"

phenomenon observed in the β Pic inner disk (Beust & Valiron 2007). For systems with a particularly high level of excess, these could be experiencing an elevated level of cometary activity due to a recent major dynamical instability such as the late heavy bombardment that happened early in the history of our own planetary system (Gomes et al. 2005).

However, another important result from the KIN observations of stars with FIR excesses, even considering the uncertainty on the shape of the zodi distribution and the derived maximum likelihood parameters, is that a large fraction of these stars appear to have zodi levels between 100 and 400 zodis, i.e., just below the KIN detection threshold. This result provides important constraints on the physical mechanism causing the emission. Once again, it appears to rule out transient phenomena such as recent local collisions which would be expected to result in a sudden brightening followed by a slow decay leading to a distribution with more faint excesses than bright ones (Kennedy & Wyatt 2013), and the inferred distribution is more compatible with the steady passing of comets from the outer belt into the inner regions. However, it is unclear why there would be a common zodi level for all stars, unless this is related somehow to the sample selection, e.g., if the ratio of zodi to cold dust is constant and the sample has uniform cold dust properties. Since the sample cold dust levels are not identical and the cometary flux depends on the scattering properties of the underlying planetary system (Bonsor et al. 2012) which is likely to show some diversity, this cannot be the sole explanation. One possibility could be that a common level arises from the physics of dust production; e.g., the balance of collisions and Poynting-Robertson (P-R) drag means that dust levels close to the star in this regime are independent of many of the properties of the outer belts (Wyatt 2005; van Lieshout et al. 2014). Indeed, such a model predicts that the brightest outer disks all converge to similar optical depth in the inner disk, i.e. the same MIR brightness, only with small variation versus spectral type. Figure 10 shows the 8.5 μm disk fractional flux expected as a function of the temperature of the outer cold dust using the simplified approach developed by Wyatt (2005). In this model, dust produced in the outer belt is of single size, and the inner dust spatial distribution and its MIR emission are solely governed by the balance between grain collisions and P-R drag, with an assumed β parameter of 0.5. In this case, all grains have the size of the smallest particles that can remain bound to to the star. Assuming a Mie scattering coefficient Q_{PR} of 1 (which is strictly valid for grains $>>$ 1 μm), this particle size can be directly derived from the stellar luminosity and mass, and from the grain density (see equation 6 of Wyatt et al. (2007)). Assuming silicate dust grains, we get for instance a grain size of 15 microns around Vega (A0V star) and 2 microns around 10 Tau (F8V). This gives an idea of the range of dust grain sizes expected from this model for most targets in our cold excess sample (11 A and F stars out of 16). For lower mass stars, the simple analytical relation from Wyatt et al. 2007 is no longer valid, and $Q_{PR} < 1$ to such an extent that it is not always possible to blow particles out, e.g. as shown by Sheret et al. (2004) in the case of ϵ Eri. Grains around these stars might then be very tiny, i.e. smaller than a micron. The displayed model curves are computed for a cold disk optical depth of 10^{-4}, but any value above $\simeq 10^{-5}$ would predict similar MIR fractional fluxes. The KIN measurements for the 16 stars with a cold outer dust belt are shown for comparison. In order to convert the observed KIN excesses into a physical excess, a zodi brightness distribution must be assumed, and we adopted a solar system-like distribution to do so (Kelsall et al. (1998), together with zodipic model). For the cold dust temperature, we used the values derived from Spitzer and Herschel excess measurements at 24, 70, 100 and 160 μm, assuming a single dust belt radius. These temperatures are listed in Table 2, together with appropriate references to MIR/FIR excess observations for each star. Despite the simplicity of this model, in particular its assumption of single-sized dust grains, and although the dependence on the outer disk temperature appears even weaker than expected, the KIN measurements are reasonably consistent with

the model predictions. In particular, the higher fractional flux level observed around A stars is predicted by the model, as well as the clustering of MIR excesses around $F_d/F^* = 1\%$ or slightly less, close to the KIN detection limit. A clear outlier is again η Crv, whose warm dust is not believed to be generated by P-R drag (Wyatt et al. 2007). While the agreement with this mechanism is reasonable, it is clear that silicate emission features and many other system specific aspects, e.g, planetary configurations (Moro-Martin et al. 2005) may also change this simple picture. Nevertheless, the close agreement of the model with the observations shows that the MIR excesses observed by the KIN plausibly have their origin in P-R drag, which in turn implies that the majority of systems with FIR excesses may have MIR excesses at levels not far below the KIN detection threshold.

A possible way to further discriminate between a cometary delivery mechanism (which the presence of massive inner planets may facilitate) and this P-R drag dust transfer scenario (possibly inhibited by such planets) would be to correlate the observed KIN excess with the presence and detailed characteristics of planetary systems around the KIN sample stars. Radial velocity exoplanetary surveys have examined twenty of the KIN targets (e.g., Fischer et al. (2014)). They identified planetary candidates around 8, revealing a wide range of system configurations with short period hot Jupiters (τ Boo, υ And), jovian planets in wider orbits (47 UMa, υ And, κ Crb and possibly ϵ Eri), Saturn-mass planets (61 Vir), together with some indication of multiple rocky planets (τ Ceti, Tuomi et al. (2013)) and long term RV trends. While none of these 8 FGK stars with RV planets show a bona fide KIN excess, this only shows a lack of correlation with a large MIR excess at $\simeq$ 500-1000 times the solar level. A detailed statistical study (similar to section 4.6) of the correlation of the measured KIN zodi level with planetary characteristics would be required to draw conclusions at lower zodi levels. However, such an analysis is difficult given the observed diversity of systems configurations and the limited number of targets showing common planetary features, and is left for potential future work.

4.7.2. Hot dust phenomenon

Interestingly, a mid-infrared excess is only detected around A stars with a cold reservoir of dust (7 out of the 11 A stars in the sample). This is opposite to the NIR observations of Absil et al. (2013), who found that A stars showed NIR excesses more frequently when they had *no* FIR excess reported. This could indicate, at least for A stars, that the physical mechanism responsible for the MIR and NIR excesses are different. In fact, only 1 out of 11 stars with a $\simeq 1\%$ NIR excess (β Leo) shows a corresponding KIN excess in the 8 to 9 μm bin, and it does have a cold FIR excess as well. Restricting the analysis to stars having only a hot excess leaves only 4 stars (all A type) and none of them show a KIN excess, suggesting again a different physical origin (non-dusty?) for the NIR excess. On the other hand, if the NIR excess emission also originates in dust, it must consist of grains hot enough to contribute a significant flux at 2μm, but small enough to have low emissivity at 9 μm and remain undetected by the KIN. However, such small grain populations should be rapidly expelled from the system, typically in a few years or so. Their presence around a large fraction of mature stars is then surprising (Absil et al. 2013), as it calls for inordinate dust replenishment rates or poorly understood dust trapping mechanisms and dynamical effects close to the star. The origin of this NIR excess / hot dust phenomenon remains then quite mysterious, and the elucidation of this problem is beyond the scope of this work. In any case, the mechanism responsible for the NIR emission does not seem to produce any significant emission in the mid-infrared, at least down to the KIN detection limit of a few 100 zodis (1σ).

5. Individual stars

From the previous analysis, 5 stars show a significant ($> 3\ \sigma$) excess in either of the two KIN spectral ranges considered, while 3 more stars appear good candidates for an excess.

5.1. Stars with detected KIN excesses

Overall, five stars show an excess leak detected at 3 σ or higher in the 8 to 9 μm bin. Only two of them (η Crv and ζ Lep) show a broad-band excess formally detected as well ($S_{cor} > 3$, where S_{cor} is the correlated excess significance defined in section 3.6.2), but all five have a broad-band excess significance greater than 2. We give for each star a brief description of the KIN findings in terms of dust location and brightness and summarize previous infrared excess observations. Table 5 summarizes the excess leak values measured as a function of wavelength and spatial frequency for each of these stars, averaging data from different scans and epochs unless strong variations are seen over time. Further detailed modeling of individual targets is left for future analysis.

5.1.1. η Crv

The most significant KIN excess is detected around η Crv, and it has to come from within $\simeq 3$ AU (according to the IWA listed in Table 1). This object was previously known to have high levels of circumstellar dust, including detections with Spitzer/MIPS at 70 μm (Beichman et al. 2006b), Spitzer/IRS/ at $5-35\,\mu$m (Chen et al. 2006; Lisse et al. 2012) and VLTI/MIDI at $10-13\,\mu$m (Smith et al. 2009). As can be seen in Figure 1, the KIN spectrum across the N-band has adequate signal to noise to resolve the 10 μm silicate feature, which can be used to infer dust properties. The observed KIN excess also shows variability versus baseline length (Table 5). The outer disk in this object has been directly imaged (Wyatt et al. 2005; Matthews et al. 2010; Duchene et al. 2014). Thus, instead of taking the disk inclination and position angle as free parameters (zodi level estimates presented in Table 2), we may assume that the exozodiacal disk has the same orientation. Using the values derived from the Duchene et al. (2014) Herschel observations ($i_{disk} = 47°$ with $\mathrm{PA}_{disk} = 117°$), we find a zodi level of 1870 ± 211 solar zodis.

5.1.2. β UMa

While β Uma was resolved previously at 11.2 μm (Moerchen et al. 2010), no significant spectral excess had been reported iat 8-9 μm so far, and the KIN $\simeq 1\%$ excess detection is then unprecedented in this wavelength range. Excesses are consistently detected at longer wavelengths with Spitzer/MIPS at 24 and 70 μm, and with Spitzer/IRS between 30 and 34 μm (Chen et al. 2006). The circumstellar emission is also resolved by Herschel/PACS at 70 and 100 μm (Booth et al. 2013), with a very clean fit to the data obtained by a narrow dust ring at about 43 AU, and seen close to edge on (i $\simeq 84$ °) with a PA of 114 °. The KIN measurements are taken almost exactly 90° away from the plane of the disk, with 2 scans obtained at a baseline azimuth of $\simeq 20°$. They are then resolving the smaller apparent dimension of the inner zodiacal disk and could hence trace much colder / distant emission that the 200 mas field of view suggests. Assuming co-alignment with the outer ring, the derived zodi level is 390 ± 96 solar zodis

5.1.3. β Leo

Stock et al. (2010) combined nulling interferometry at 10 μm using the MMT, KIN preliminary reduction results, and photometry from 3 to 100 μm using Spitzer to study the debris disk around β Leo over a broad range of spatial scales, corresponding to radii of 0.1 to 100 AU. They derived a complex debris system with relatively little material within 1 AU, an inner component with a color temperature of 600 K fitted by a dusty ring extending from about 2 to 3 AU, and a second component with a color temperature of 120K fitted by a broad dusty emission zone extending from about 5 to 55 AU. Herschel 100 and 160 μm images confirm this picture of the outer component, deriving a 40 AU disk radius seen close to pole-on, together with a characteristic grain size smaller than 16 μm (Matthews et al. 2010). An even more complex model is proposed by Churcher et al. (2011), with inner hot dust at 2 AU, an intermediate warm dust belt at 9 AU and a colder component extending from 30 to 70 AU. Given the inner and outer working angles of the KIN, the detected MIR excess must reside between 0.07 and 2.2 AU (Table 1). This is consistent with the presence of an inner ring around 2 AU, although we have no constraint on the excess spatial distribution inside of that radius. Finally, the ratio (1.041) measured between the semi-major and semi-minor disk radii of the Spitzer MIPS images (Stock et al. 2010) suggests that the disk is viewed at $20^{\circ}\pm 10^{\circ}$, close to face-on, which is consistent with the measured stellar inclination of 21.5°(Akeson et al. 2009). Adopting this inclination value for the inner component detected by the KIN, we derive a zodi level of 301 $\pm$ 75.

5.1.4. ζ Lep

ζ Lep has long been known for its 12 μm IRAS excess indicative of dust material at unusually high temperature in the immediate vicinity of the star (Aumann & Probst 1991). Infrared excesses have also been reported around this star at 24 and 70 μm by SPITZER/MIPS yielding a [24] - [70] dust color temperature of 206 K (Su et al. 2006), fairly close to the 191 K $\pm$ 3 K derived from a single black-body fit to the SPITZER IRS spectrum measured between 5.5 and 35 μm (Chen et al. 2006). The conversion of these SED derived apparent dust temperatures to actual dust location is however difficult without a proper knowledge of the grain basic properties, such as composition and size distribution. This was recently evidenced by Herschel spatially resolved observations of debris disks, showing dust location at significantly (up to 2.5 times) larger distance than predicted by simple blackbody fits to their SEDs (Booth et al. 2013). Prior attempts to directly resolve the warm disk component around ζ Lep have placed the warm dust component as close as 3 AU from the star, using T-ReCS Gemini South observations at 10.4 μm and 18.3 μm (Moerchen et al. 2007), and most likely $\leq$ 6AU based on early Keck images obtained at 11.7 and 17.9 μm (Chen & Jura 2001). Our resolved KIN observations are quite revealing in that respect, as they only show a $\simeq$ 1% leak excess, i.e., much smaller than the 13.6% mean IRS excess detected between 8.5 and 13 μm (Chen et al. 2006) which has a typical rms uncertainty of $\simeq$ 1% in that wavelength range (Lawler et al. 2009). Even if the IRS excess is weaker (around 5-10%) at the short (8 to 10μm) wavelength end that the KIN is mostly sensitive to, these two measurements are very difficult to reconcile. While we can not formally rule out a substantial emission arising from within the 0.15 AU KIN IWA, the most likely explanation is that most of the IRS-N band excess flux actually comes from regions outside of the KIN $\simeq$ 4 AU field of view. Such a location would also be in line with recent 2-belt modeling of warm debris disks IRS spectra by Ballering, Rieke & Gaspar (2014), which used emission features to derive additional information about the grain properties, and found a best fit inner belt location of 5 to 6 AU in the case of ζ Lep (significantly larger than the $\simeq$

3 AU previously suggested). Assuming a disk inclination of 30° with a PA of 50°, consistent with the Gemini South resolved observations of Moerchen et al. (2010), we find a zodi level of 243 ± 73 solar zodis.

5.1.5. γ Oph

This star was previously known to have excess starting at $\simeq$ 15 μm, and growing much larger at longer wavelengths (Spitzer IRS spectrum analysis, Chen et al. (2006); Su et al. (2008)). It was listed as a possible KIN excess source in Paper I, and this new analysis confirms the presence of a small mid-infrared excess around 10 μm. It is noteworthy that while the FIR excess emission is known to be larger around γ Oph than around η Crv (Duchene et al. 2014), the circumstellar excess is much weaker at 10 μm around γ Oph. This relative lack of inner warm dust is evidenced both by our KIN resolved measurements and by SPITZER IRS spectra, pointing to different spatial distributions around the two stars, with little dust within 5-10 AU in the case of γ Oph. The Spitzer images (Su et al. 2008) also spatially resolved the outer disk, suggesting a disk radius of $\simeq$ 520 AU at 70 μm and $\geq$ 260 AU at 24 μm, yielding an inclination of 50° and a PA of 55°. Assuming the same orientation for the exozodi disk, we derive a level of 290 ± 94 zodis.

5.2. Stars with likely or "candidate" KIN excesses

As discussed in Section 4, the measured histograms of excess significance and zodi levels are strongly skewed towards higher detection levels. They show an excess of about 10 to 15 stars over what would be expected from random gaussian measurement noise. Among them, a number of stars lie close to the KIN detection limit, at the 1 to 3 σ confidence levels. All of these stars are reasonable candidates for a MIR excess and will be particularly interesting to observe with a higher contrast instrument such as the LBTI. However, we concentrate here on KIN targets which have a broad-band correlated excess significance larger than 2, which probably really corresponds to a $\simeq 3\sigma$ excess (section 4.3). This selection criterion leaves the 5 bona fide KIN excess stars previously identified, plus three more A-type stars: Fomalhaut, Vega, and Altair. Noticeably, these 3 stars are hot and close enough that any putative dust at 300K will extend significantly further than the KIN outer working angle (Table 1). Consequently, a significant fraction of the MIR circumstellar flux might have been missed around these stars.

5.2.1. Fomalhaut

While Fomalhaut does not show any significant excess in the 8 to 9 μm bin, the measured excess leak increases at longer wavelengths, and the full N-band correlated excess is one of the highest measured in the overall sample. A separate analysis of Fomalhaut KIN observations (Mennesson et al. 2013) - which included the survey results presented here and 2007 commissioning data - concluded the presence of a small excess leak with a mean value of 0.35%± 0.10% between 8 and 11 μm. This small KIN excess is likely the short wavelength tail of the unresolved excess detected by Spitzer/IRS at slightly longer MIR wavelengths (Stapelfeldt et al. 2004; Su et al. 2013), interpreted as the signature of a warm dust ($\simeq$ 170K) component located near the water frost line, inside of $\simeq$ 10 AU. A parametric modeling of the NIR (VLTI) and MIR (KIN) Fomalhaut interferometric data complemented by spectro-photometric measurements from Spitzer and Herschel (Acke et al. 2012), concluded the existence of two distinct dust populations within a few AU

(Mennesson et al. 2013; Lebreton et al. 2013): (1) a population of very small (0.01 to 0.5 μm) and therefore unbound, hot (1500 K) dust grains confined in a narrow region ($\simeq$ 0.1 - 0.3 AU) at the sublimation rim of carbonaceous material; (2) a population of larger bound grains at about 2AU that is protected from sublimation and has a larger mass despite its fainter flux level. These previous analyses also suggested that the hot dust component may be produced by the release of small carbon grains following the disruption of dust aggregates originating from the warm component.

5.2.2. Vega

Vega has been observed more than any other star in the KIN sample: a total of 18 scans were taken over 5 different epochs (from May to August 2008) and 9 different calibrators were used, all in an attempt to beat down the systematics. While these numerous observations yielded the smallest final null measurement uncertainties (10^{-3}), excesses measured in the 8 to 9 micron bin and broad-band channels remain at the $\simeq 2\sigma$ level in both cases. While a 10 μm excess is likely (see Section 4.3), we prefer to consider Vega a "KIN excess candidate". It is obviously a prime target for further observations with the LBTI nuller, as only a minor gain in accuracy, or a larger field of view, could either confirm or rule out this candidate excess. We also note that due to its limited field of view ($\simeq$ 1.5 AU radius at Vega's distance), the KIN may have missed a large fraction of dust emission at 300K or lower (Table 1). Since the Vega system is seen nearly pole -on (Monnier et al. 2012), the KIN observations are in particular completely insensitive to dust at 170K ($\simeq$ 14 AU), the temperature derived from Spitzer/IRS spectrum analysis (Su et al. 2013). In any case, the KIN leak excess (3σ) upper limit is about 0.5%, which translates into a maximum physical excess of about 1% within the instrument field of view. [10] Once again, this result is quite surprising given the $\simeq$ 1% NIR excesses previously reported around Vega by various interferometers (CHARA: Absil et al. (2006), IOTA: Defrere et al. (2011)). Assuming no temporal variability of the excess between the NIR CHARA/IOTA and MIR KIN measurements, it would have to originate in very hot dust grains located close to the star, yet small enough to remain largely undetected at 10 μm (Mennesson et al. 2011).

5.2.3. Altair

Altair has no excess reported at either 24 or 70 μm (Gaspar et al. 2013). A solidly significant mid-infrared KIN excess would then be particularly interesting as it would be the only one detected around a star with no prior evidence of an outer cold dust reservoir. It is noteworthy that out of the 25 stars with data presented in Paper I, only Altair shows significantly different results in this new reduction (Table 2). While Paper I reported a marginal excess between 8 and 9 μm, we find no evidence for it here. The reason is that a single calibrator (HD 184406) was used for Altair null measurements presented in Paper I, and its diameter was apparently wrongly estimated from the FATCAT KI measurements, causing an overestimation of Altair's calibrated null depth. Indeed, Paper I used a uniform disk (UD) diameter of 3.05 $\pm$ 0.07 mas for HD 184406, while we use here the smaller UD diameter of 2.25 $\pm$ 0.06 mas measured in October 2013 by the CHARA interferometer (Nic Scott, private communication). Note that this new value is in remarkable agreement with

[10]The exact scaling factor between the 2 excess quantities depends on the spatial distribution of the excess, but over a wide range of possible models (e.g., , thin annular ring or uniform emission inside the KIN field of view), the conversion factor is about 2.

the K band UD diameter of 2.24 ± 0.02 mas estimated from precise SED fitting of interferometric calibrators (Borde et al. 2002). The revised calibrator diameter value strongly reduces the excess leak measured at short wavelengths (8 to 9 μm bin), but this calibration effect is less at longer wavelengths, and we still find a rather large excess significance (2.55) for Altair's broad-band 8 to 13 μm excess. The excess spectral shape is also reminiscent of that found around Fomalhaut, steadily increasing with wavelength. Another difficulty in assessing a possible excess around Altair is that the star is large enough that uncertainties on its angular diameter can result in significant errors on the excess leaks derived. Altair's photosphere is known to be elongated due to fast rotation (van Belle et al. 2001). Even though we took this effect into account and adopted the diameter measured at H-band by the CHARA MIRC instrument (Monnier et al. 2007) over the range of position angles sampled by our observations (3.64 mas ± 0.03 mas), we recognize that the N-band diameter may be significantly different, especially in the presence of strong gravity-induced limb darkening. For this reason, and although the existence of a small MIR excess is possible, there might be some residual calibration issues for Altair, and we also prefer to classify it as a "KIN excess candidate".

6. Conclusions

A total of 47 stars have been surveyed by the Keck Interferometer Nuller (KIN) between 2008 and 2011, including 40 stars with no known companion within the instrument field of view. The overall data have been reduced in a common manner, allowing an assessment of the amount of resolved off-axis emission above the stellar photosphere as a function of wavelength between 8 and 13 μm. Only five stars show an 8 to 9 μm mid-infrared excess (η Crv, β Leo, β UMa, ζ Lep and γ Oph), while a marginal N-band excess is also detected around Fomalhaut. While the results' statistical significance is necessarily limited by the sample size, we only detect mid-infrared excesses around main sequence stars with types earlier than F2.

We find that all stars with a bona fide or candidate KIN excess had a previously detected FIR excess. A statistical analysis of the whole dataset shows a more general correlation between the level of (zodi-like) warm dust emission measured at 8 to 9 μm and the presence of (Kuiper-like) cold dust. While warm dust detected by the KIN necessarily resides within the inner few AU, it thus likely finds its origin in the outer regions of the system rather than through in-situ collisions of large parent bodies. We also found that stars with previously known cold FIR excesses generally have zodi levels close to the KIN detection limit of a few 100 zodis (1 σ). This observation is broadly consistent with a scenario where an outer planetesimal belt is feeding dust to the inner system through the balanced effects of P-R drag and grain collisions, which predicts that the level of warm dust emission is fairly insensitive to the properties of the outer disk, as long as it is bright enough. These cold excess stars constitute prime science targets for higher precision / larger field of view MIR observations of exozodiacal dust, but are probably bad targets for future missions designed to directly image Earth analogues.

We also find that stars with a NIR excess recently reported by interferometry do not show any corresponding excess detectable by the KIN. This lack of correlation could either point to a different mechanism for the generation of the NIR circum-stellar emission, or call for large amounts of very hot grains piling up close to the sublimation radius of these stars, small enough to have a low MIR emissivity and remain undetected by the KIN.

Finally, assuming that the 20 solar type stars with no previously detected IR excess observed by the KIN constitute an independent and identically distributed sample, and testing a wide range of reasonable shapes

for the underlying distribution, we find a most likely median zodi level of 20 zodis or less for these stars. Assuming a log-normal zodi luminosity function, we further established with high confidence (95%) that at least 50% of such stars have zodi levels lower than 60 zodis. This is potentially good news for a future direct exo-Earth imaging mission, although an exo-zodiacal cloud at 60 times the solar level is still problematic. MIR observations of a larger sample with lower detection limits is then still desirable for the proper design of such missions and optimum target selection.

7. Acknowledgements

The Keck Interferometer was funded by the National Aeronautics and Space Administration (NASA). Part of this work was performed at the Jet Propulsion Laboratory, California Institute of Technology, and at the NASA Exoplanet Science Center (NExScI), under contract with NASA. The Keck Observatory was made possible through the generous financial support of the W.M. Keck Foundation. This research has made use of the Washington Double Star Catalog maintained at the U.S. Naval Observatory. MCW is grateful for support from the European Union through ERC grant number 279973.

8. Appendix 1: KIN Observable

Four beams are recombined by the KIN system (Colavita et al. 2009). A split mirror located downstream of each Keck telescope adaptive optics system—close to a pupil plane—divides the light gathered by each telescope into "left" and "right" beams. Long baseline (85 m) interferometric recombination first occurs separately between the two left beams, and between the two right beams, with each beam pair either recombined constructively (at peak) or destructively (at null). The resulting left and right output fields are then coherently recombined using a standard Michelson interferometer, called the "cross-combiner". As the optical delay is rapidly scanned inside the cross-combiner, one measures a fringe amplitude with left and right beam pairs at null, and then with left and right beam pairs at peak. The null depth is defined as the ratio of the cross-combiner fringe amplitudes obtained at null and at peak, and is measured in each of ten independent spectral channels covering the full N band (8 to 13 μm). The rationale for this complex 4-beam combination and modulation is that the resulting measured null depth is free of slow drifts in the incoherent background (Mennesson et al. 2005; Serabyn et al. 2012), a source of strong potential bias for ground-based interferometric observations in the thermal IR. Two different scales and baselines are then at play: the interferometric nulling baseline of length $B \simeq 85$ m, separating the telescopes centers, and the short cross combiner baseline $b \simeq 4$ m, characteristic of the interference between the "left" and "right" parts of a given Keck telescope.

For a perfectly calibrated instrument, defined as providing a null depth of zero on a point source, the measured monochromatic astrophysical null $N_{\rm ast}$ can be related to the source brightness distribution on the sky $I(\vec{\theta})$ via (Serabyn et al. 2012; Mennesson et al. 2013):

$$N_{\rm ast}(\lambda) = \frac{\int I(\vec{\theta}) \sin^2(\pi \vec{B} \cdot \vec{\theta}/\lambda)) \cos(2\pi \vec{b} \cdot \vec{\theta}/\lambda) \sqrt{T_L(\vec{\theta}) T_R(\vec{\theta})} d\vec{\theta}}{\int I(\vec{\theta}) \cos^2(\pi \vec{B} \cdot \vec{\theta}/\lambda) \cos(2\pi \vec{b} \cdot \vec{\theta}/\lambda)) \sqrt{T_L(\vec{\theta}) T_R(\vec{\theta})} d\vec{\theta}} \,, \tag{17}$$

where $T_L(\vec{\theta})$ and $T_R(\vec{\theta})$ designate the sky transmission of the left and right Keck beams, respectively. These

are computed from the telescopes orientation and from the overall beam train propagation, which includes an intermediary focal plane pinhole limiting the geometric field of view radius to 300 mas. As shown in Equation 17, in the case of an extended source, the measured null level is not only affected by the long baseline nulling pattern (fast oscillating squared sine term), but also by the cross fringe pattern (slowly oscillating cosine term) and by the lobe antenna of each single beam. The overall transmission pattern of the KIN is illustrated in Fig. 11, showing the case of Fomalhaut observations at the time of meridian transit. Taking into account the individual beam transmission (finite field of view) and cross combiner modulation effects (small baseline b), the source brightness distribution effectively seen by the KIN can be written as:

$$I_{KIN}(\vec{\theta}) = I(\vec{\theta}).\sqrt{T_L(\vec{\theta})T_R(\vec{\theta})}.\cos(2\pi\vec{b}\cdot\vec{\theta}/\lambda) \tag{18}$$

The corresponding interferometric visibility measured at baseline $\vec{B}$ is defined by:

$$V_B = \frac{\int I_{KIN}(\vec{\theta}).e^{(j2\pi\vec{B}\cdot\vec{\theta}/\lambda)}d\vec{\theta}}{\int I_{KIN}(\vec{\theta}).d\vec{\theta}} \tag{19}$$

Replacing in Equation 17, one finally obtains after some little algebra:

$$N_{\rm ast}(\lambda) = \frac{(1-|V_B|)}{(1+|V_B|)} \tag{20}$$

This is the usual relation between astronomical null depth and visibility, except that the null or visibility is measured here for a "modified" source brightness distribution, which incorporates both the KIN instrument limited field of view *and* the short baseline cosine modulation (Equation 18).

9. Appendix 2: Confidence intervals for parameters estimated by Maximum Likelihood method

Given the maximum likelihood function L defined in section 4.6.2., and the maximum likelihood parameters $\hat{\vec{\theta}} = (\hat{\theta_1}, \hat{\theta_2}, ..., \hat{\theta_p})$, we define the profile likelihood function for a single parameter of interest, e.g. θ_1, as (Venzon & Moolgavkar 1988):

$$R(\theta_1) = \frac{\max\limits_{(\theta_2,...,\theta_p)} L(\theta_1, \theta_2, ..., \theta_p)}{L(\hat{\vec{\theta}})} \tag{21}$$

where the numerator is simply, for each value of parameter θ_1, the maximum of the likelihood function over the remaining parameters (if any). For a large enough sample (asymptotic normal assumption), the quantity X^2= -2 ln R(θ_1) follows a chi-square distribution with one degree of freedom (Venzon & Moolgavkar 1988), meaning that X follows a unit normal distribution. This property allows us to compute confidence intervals for each of the derived maximum likelihood parameters, which is much preferable to giving 1σ uncertainties with no confidence levels attached to them. A 100(1-α)% likelihood-based confidence interval for θ_1 is obtained for the set of θ_1 values verifying:

$$R(\theta_1) \geq exp(-\chi^2_{(1-\alpha;1)}/2) \tag{22}$$

For example, a (2-sided) 90% confidence interval (95% on upper or lower bounds), corresponds to a χ^2 value of 2.706, and the condition is then that $R(\theta_1)$ be higher than 0.259. This method is used to compute confidence intervals for the maximum likelihood parameters derived in section 4.6.2. and for the (profile) likelihood curves shown in figures 6, 7, & 8.

An other possible approach, which does not rely on the asymptotic normal assumption, is to compute Bayesian confidence bounds for a given parameter by integrating its marginal distribution given the data. In the case of a log-normal distribution with parameters (μ,σ), the confidence level for a given upper limit μ^u on parameter μ is given by:

$$P(\mu \leq \mu^u) = \frac{\int_{-\infty}^{\mu^u} \int_0^{\infty} (L(\mu,\sigma)/\sigma)\ d\sigma\ d\mu}{\int_{-\infty}^{\infty} \int_0^{\infty} (L(\mu,\sigma)/\sigma)\ d\sigma\ d\mu} \tag{23}$$

As an independent check, we applied this Bayesian approach to the likelihood function L computed for the ensemble of solar type stars with no excess previously detected (Group 1), assuming a log-normal zodi distribution. Using the above equation to compute confidence levels for the distribution μ parameter, we found values very similar to those presented in Section 4.6.4: the ensemble median zodi level ($\exp(\mu)$) upper limit is 55 solar zodis at 95% confidence, and 90 zodis at 99% confidence.

REFERENCES

Absil, O. et al. 2006, A&A, 452, 237

Absil, O. et al. 2009, A&A, 704, 150

Absil, O. et al. 2011, A&A, 535, 68

Absil, O. et al. 2013, A&A, 555, 104

Acke, B. et al. 2012, A&A, 540, 125

Akeson, R. L. et al. 2009, ApJ, 691, 1896

Aufdenberg, J. P. et al. 2006, ApJ, 651, 617

Aumann, H.H. & Probst, R.G. 1991, ApJ, 368, 264

Backman, D. et al. 2009, ApJ, 690, 1522

Ballering, N., Rieke, G.H¿ & Gaspar, A., Astro-ph, arXiv1407.7547, accepted for publication in the ApJ

Beichman, C. A. 2005, ApJ, 626, 1061

Beichman, C. A., et al. 2006a, ApJ, 652, 1674

Beichman, C. A., et al. 2006b, ApJ, 639, 1166

Beust, H. and Valiron, P. 2007, A&A, 466, 201

Boden, A. F., et al. ApJ, 515, 356

Bonneau, D. et al. 2006, A&A, 456, 789

Bonsor, A., Augereau, J.-C., Thebault, P. 2012, A&A, 548, 104

Bonsor, A. and Wyatt, M. C. 2012, MNRAS, 420, 299

Bonsor, A., et al. 2013, MNRAS, 431, 3025

Bonsor, A. et al. 2014, MNRAS, 441, 2380

Booth, M. et al. 2013, MNRAS, 428, 1263

Borde, P. et al. 2002, A&A, 393, 183

Bryden, G. et al. 2009, ApJ, 705, 1226

Burgasser, A. et al. 2003, ApJ, 586, 512

Chen, C. H. and Jura, M. 2001, ApJ, 560L, 171

Chen, C. H., et al. 2006, ApJS, 166, 351

Churcher, L. J. et al. 2011, MNRAS, 417, 1715

Cohen, M. et al 1999, AJ, 117, 1864

Colavita, M. M., et al. 2009, PASP, 121, 1120

Colavita, M. M., et al. 2013, PASP, 125, 1226

Defrere, D. et al. 2011, A&A, 534, 5

Duchene, G. et al. 2014, ApJ, 784, 148

Di Benedetto G. P. 2005, MNRAS, 357, 174

Dodson-Robinson, S. E,, Beichman, C. A., Carpenter, J. M., & Bryden, G., 2011, AJ, 141, 11

Eiroa, C. et al. 2013, A&A, 555, 11

Fujiwara, H. et al. 2012, ApJ, 759, 18

Fischer, D. et al. 2014, ApJS, 210, 5

Gaspar, A., Rieke, G., Zoltan, B., 2013, ApJ, 768, 25

Gomes, R., Levison, H. F., Tsiganis, K., Morbidelli, A. 2005, Nature, 435, 466

Habing et al. 2001, A&A, 365, 545

Hartkopf, W. I., Mason, B. D., & Morley, C. E. 2001, Sixth Calaog of Orbits of Visual Binary Stars, http://ad.usno.navy.mil/wds/orb6/orb6text.html

Gezari et al. 1993, NASA Ref. Pub. 1294, Cat. of Infrared Observations

Hale, A. 1994, AJ, 107, 306

Kalas, P. et al. 2008, Science, 322, 5906, 1245

Kelsall, T. et al. 1998, ApJ, 508, 44

Kennedy, G. M. and Wyatt, M. C. 2013, MNRAS, 433, 233

Koenig, B. et al. 2002, A&A, 394, 43

Lagrange, A.-M. et al. 2009, A&A, 493L, 21L

Lawler, S. M. et al. 2009, ApJ, 705, 89

Lebreton, J. et al. 2013, A&A, 555, 146

Lisse, C. M. et al. 2012, ApJ, 747, 93

Macintosh, B. et al., accepted for publication Proc. Natl. Acad. Sci, arXiv:1403.7520

Mason, B. D. et al. 2001, AJ, 122, 3466

Matthews, B. C. et al., 2010 A&A, 518L, 135

Merand, A. et al. 2006, A&A, 447, 783

Mennesson, B., Leger, A., Ollivier, M. 2005, Icarus, 178, 570

Mennesson, B. et al. 2011, ApJ, 736, 14

Mennesson, B. et al. 2013, ApJ, 763, 119

Millan-Gabet, R. et al. 2011, ApJ, 734, 67

Moerchen, M. M.et al. 2007, ApJ, 655L, 109

Moerchen, M. M., Telesco, C. M., Packham, C. 2010, ApJ, 723, 1418

Monnier, J. D. et al. 2007, Science, 317, 342

Monnier, J. D. et al. 2012, ApJ, 761, 3

Moro-Martin, A., Wolf, S. & Malhotra, R. et al. 2005, ApJ, 621, 1079

Neugebauer, G. & Leighton, R. B. 1969, Two-Micron Sky Survey: A Preliminary Catalog, NASA SP-3047

Nesvorny, D., Jenniskens, P., Levison, H. F., Bottke, W. F., Vokrouhlicky, D. & Gounelle, M., 2010, ApJ, 713, 816

Rhee, J. H. et al. 2007, ApJ, 660, 1556

Rieke, G. H. et al. 2005, ApJ, 620, 2, 1010

Roberts, L. et al. 2011, AJ, 142, 175

Schmelling, M. 1995, Physica Scripta., 51, 676

Serabyn, G. et al. 2012, ApJ, 748, 558

Sheret, I. et al. 2004,MNRAS, 348, 1282

Smith, R., Wyatt, M. C.. & Haniff, C. A., 2009, A&A, 503, 265

Stapelfeldt, K. R. et al. 2004, ApJS, 154, 458

Stock, N. D. et al. 2010, ApJ, 724, 1238

Su, K. Y. L. et al. 2006, ApJ, 653, 1, 675

Su, K. Y. L., Rieke, G. H., Stapelfeldt, K. R., Smith, P. S., Bryden, G., Chen, C. H. & Trilling, D. E., 2008, ApJ, 679, L125

Su, K. et al. (2013), ApJ, 763, 118

Trilling, D. E. et al. 2008, ApJ, 674, 1086

Tuomi, M. et al. 2013, A&A, 551, 79

van Belle, G. T., Ciardi, D. R., Thompson, R. R., Akeson, R. L. & Lada, E. A., 2001, ApJ, 559, 1155

van Lieshout, R. et al. 2014, å, in press, arXiv1404.3271

Venzon, D.J. & Moolgavkar, S.H. 1988, Journal of Applied Statistics, 37, 87

Weinberger, A. J., Becklin, E. E., Song, I., Zuckerman, B. 2011, ApJ, 726, 72

Weinberger, A. J. et al. 2014, in preparation

Wyatt, M. C. 2005, A&A, 433, 1007

Wyatt, M. C. et al. 2005, ApJ, 620, 492

Wyatt, M. C. et al. 2007, ApJ, 658, 569

Wyatt, M. et al. 2012, MNRAS, 424, 1206

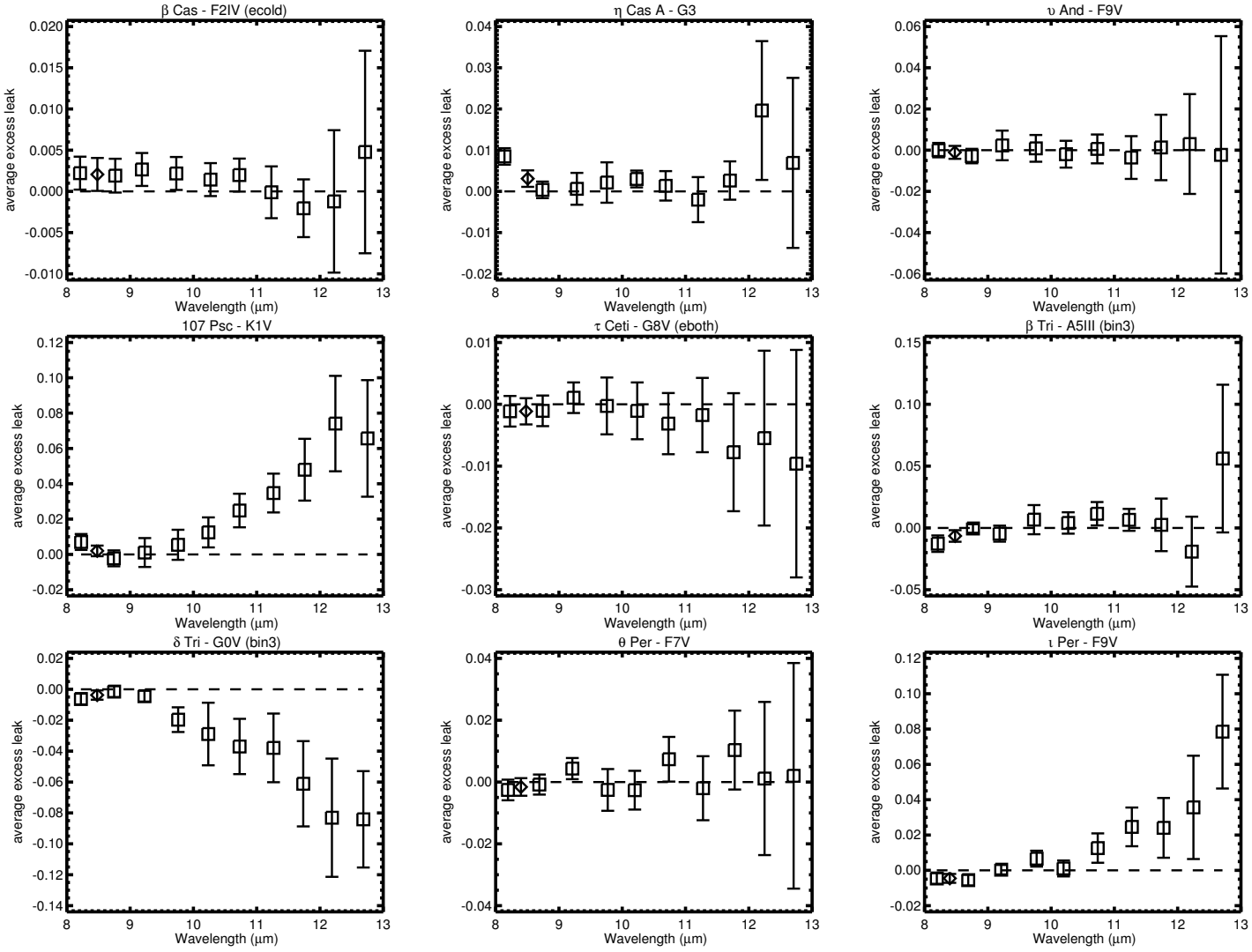

Fig. 1.— Excess leaks measured as a function of wavelength for 44 stars with no obvious stellar companion signature in the data (displayed in the same -increasing right ascension - order as in Table 1). All available measurements are averaged together to produce the curves displayed. This sample includes 38 presumably single stars, two stars with known stellar companions outside of the KIN field of view (type "bin1"), and 4 stars with known stellar companions within the KIN field of view (binary types "bin2" and "bin3"). The designations "ecold", "ehot" and "eboth" correspond to stars with known cold excess ($\lambda = 60$ to 160 μm), hot excess (around 2 μm) or both types of excess, respectively. The degradation of sensitivity at the red end of the bandpass, as discussed in the text, can be clearly seen. For the analysis presented in this paper we use both the excess measured in the $8 - 9\,\mu$m spectral bin (solid diamonds), which has the highest sensitivity for exozodi detection, and broad-band excess estimates based on the whole 8 to 13 μm range.

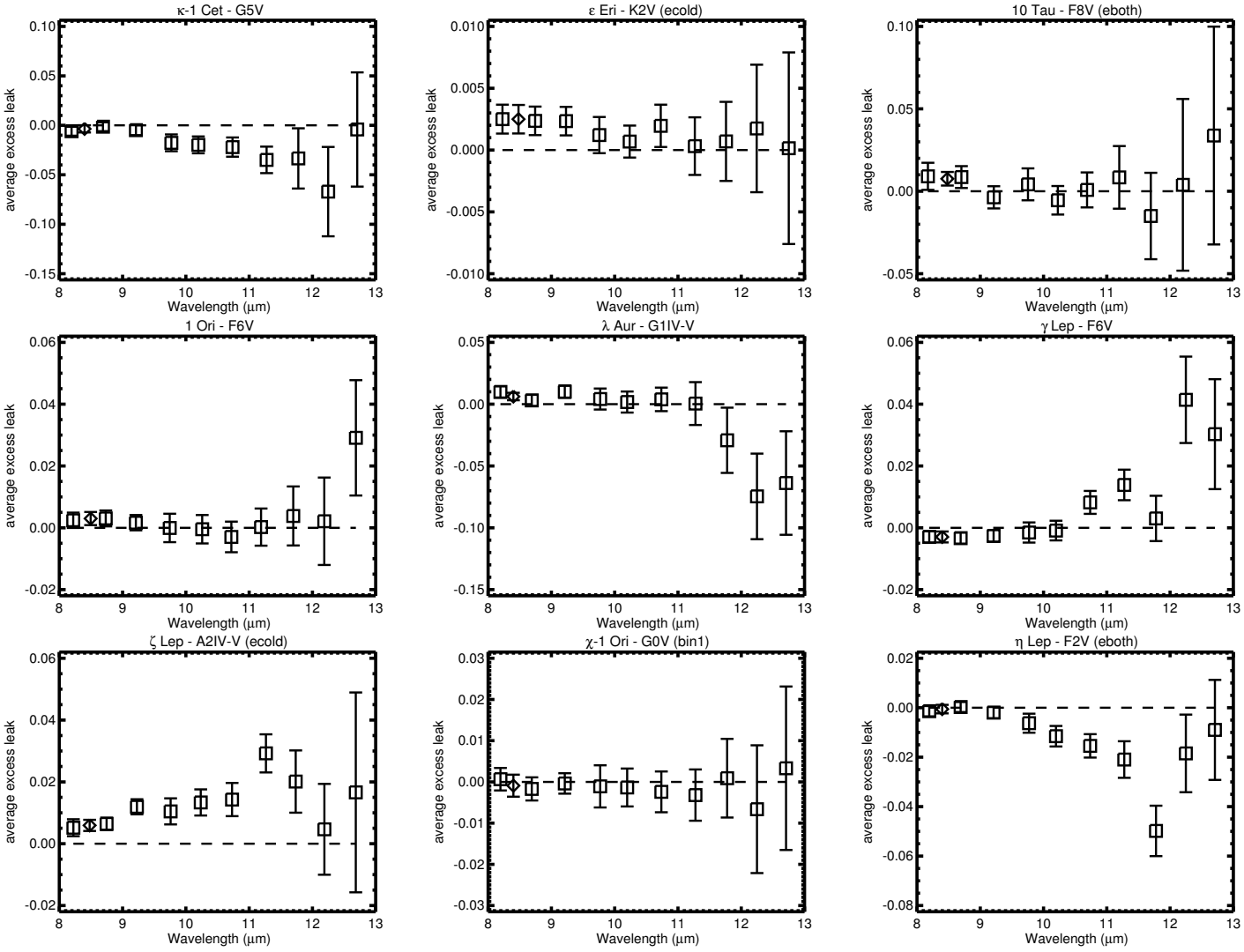

Fig. 1.— *continued*

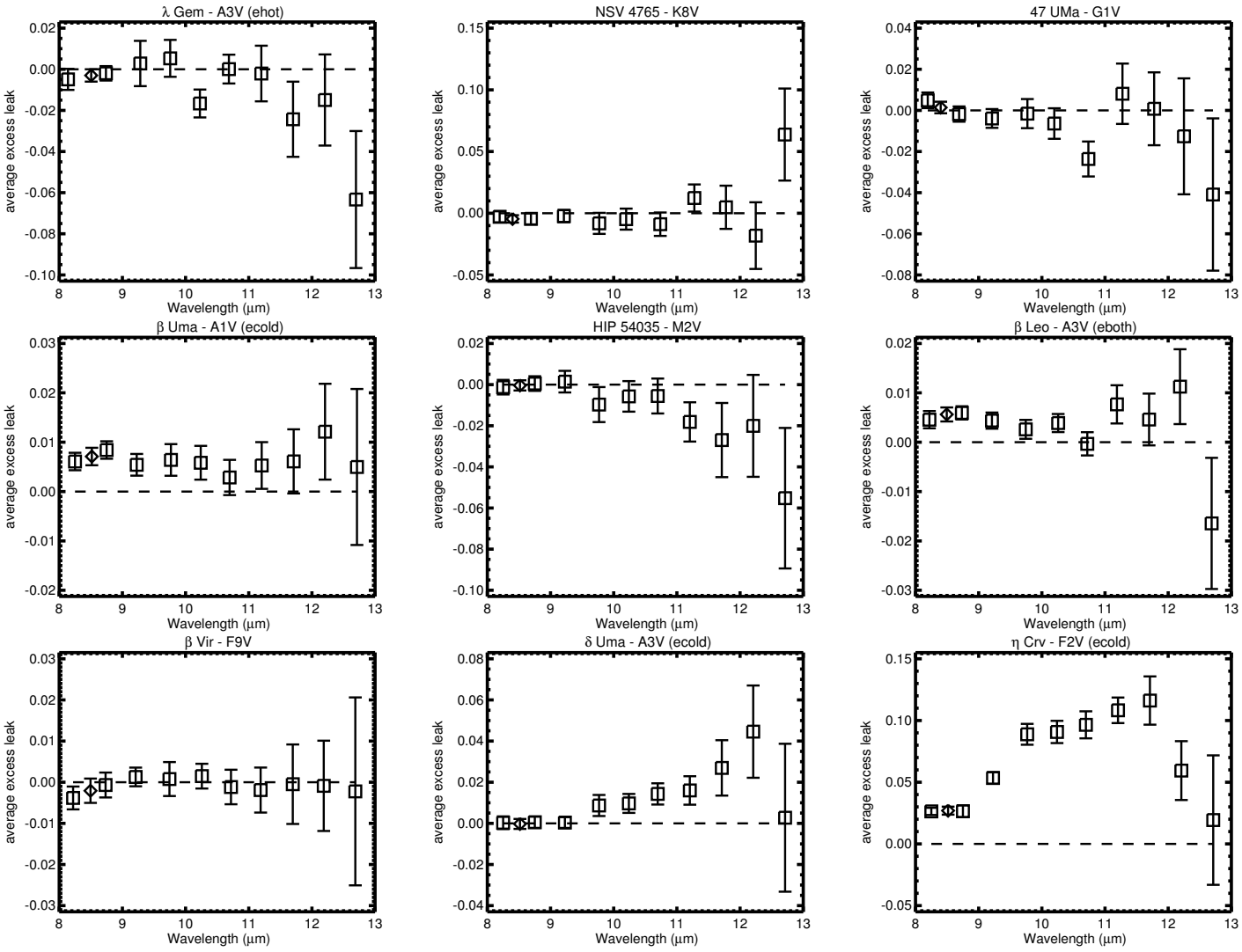

Fig. 1.— *continued*

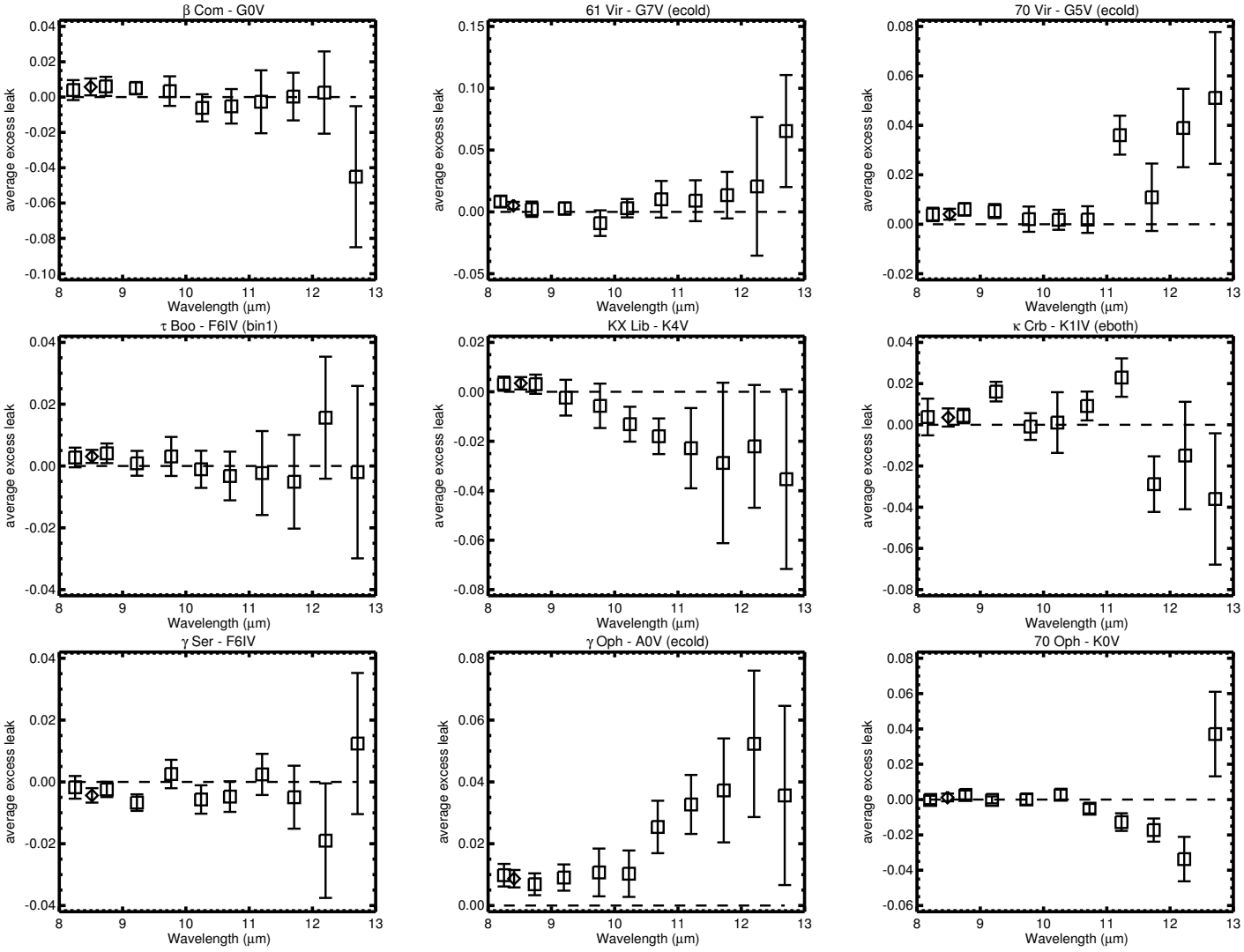

Fig. 1.— *continued*

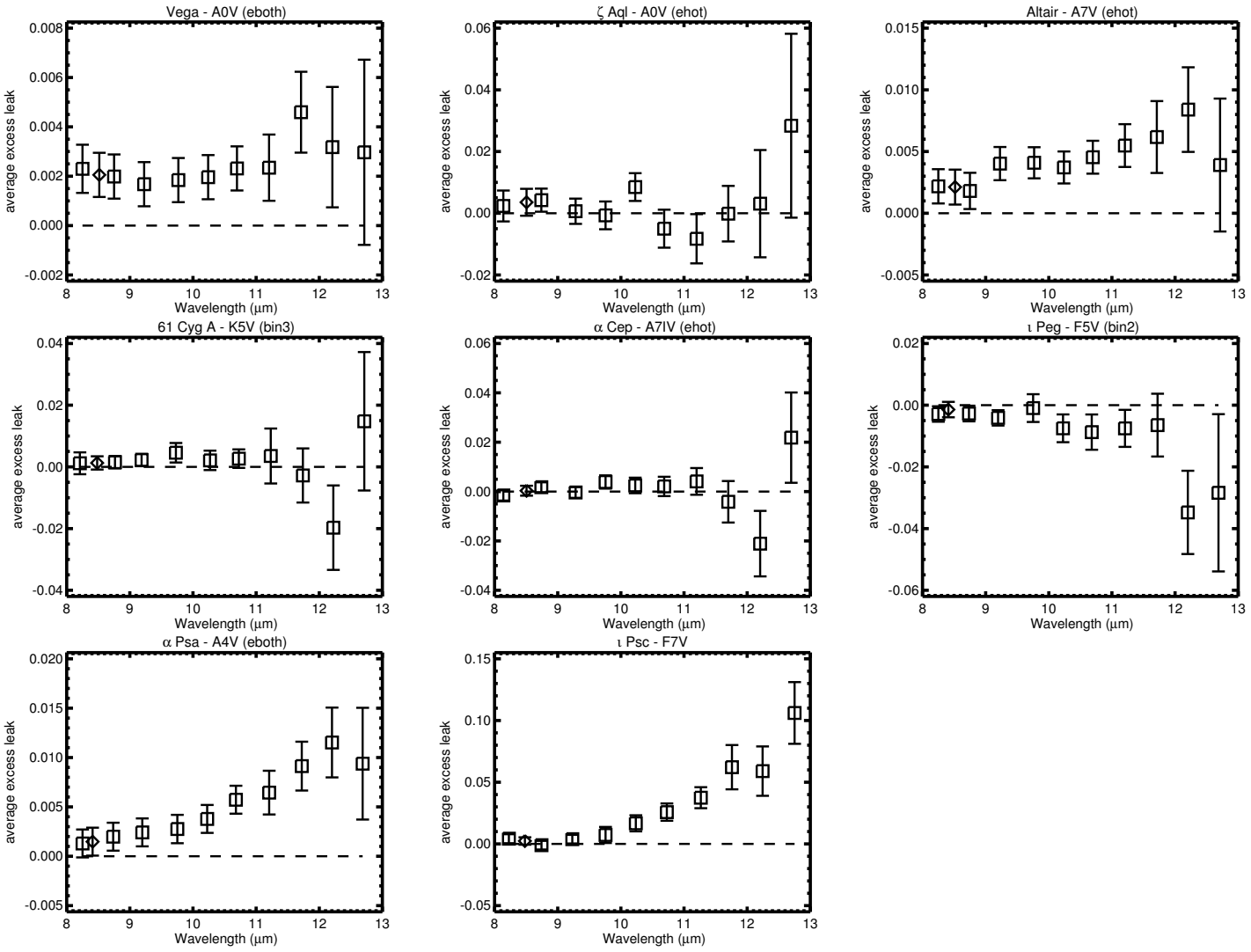

Fig. 1.— *continued*

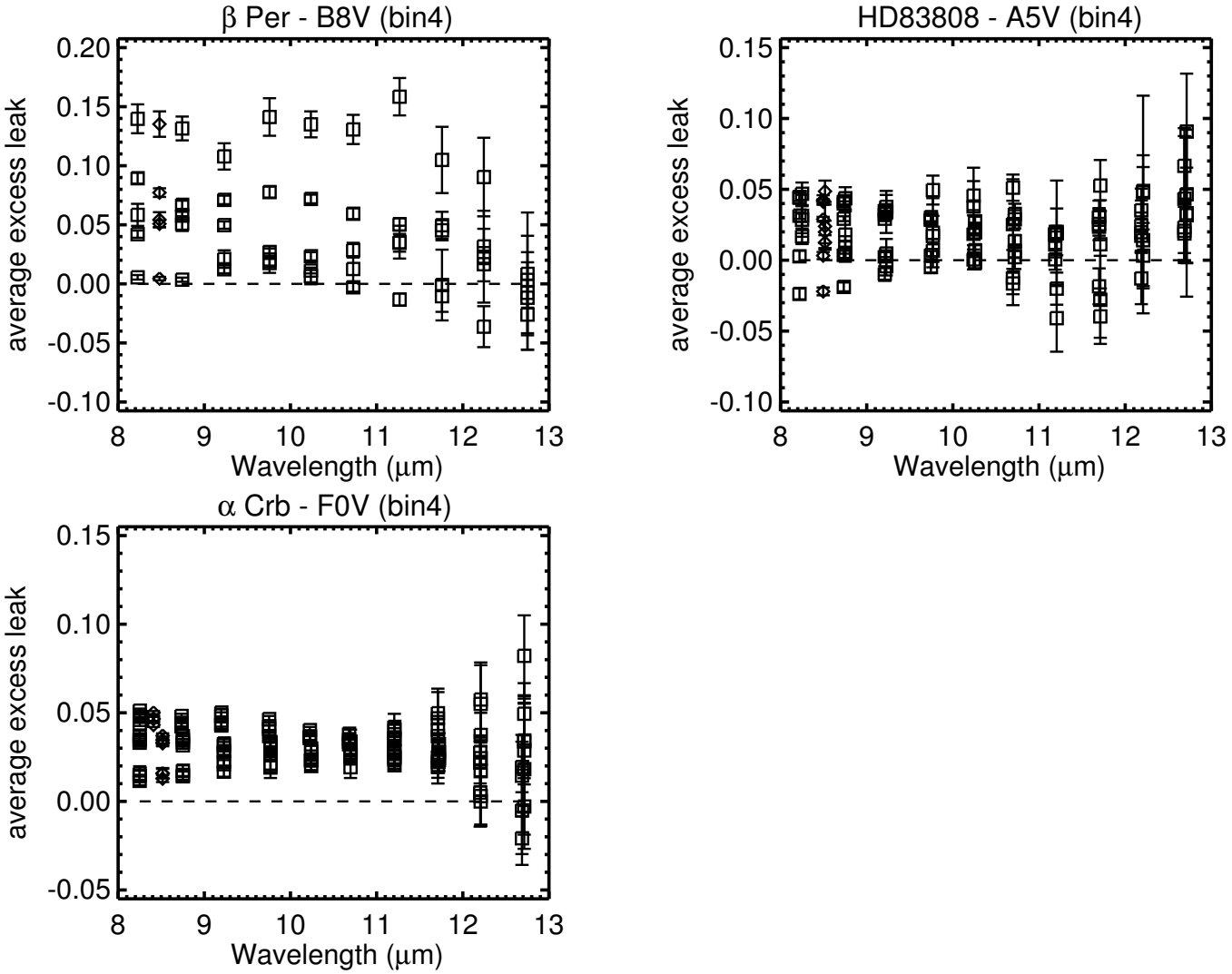

Fig. 2.— Excess leaks measured by the KIN for three stars with obvious signatures of stellar companions in the data (type "bin4"). All available measurements are displayed, showing large null fluctuations vs time and baseline azimuth. These stars have been discarded from subsequent zodiacal dust level estimations and correspond to the last 3 targets listed in Table 1.

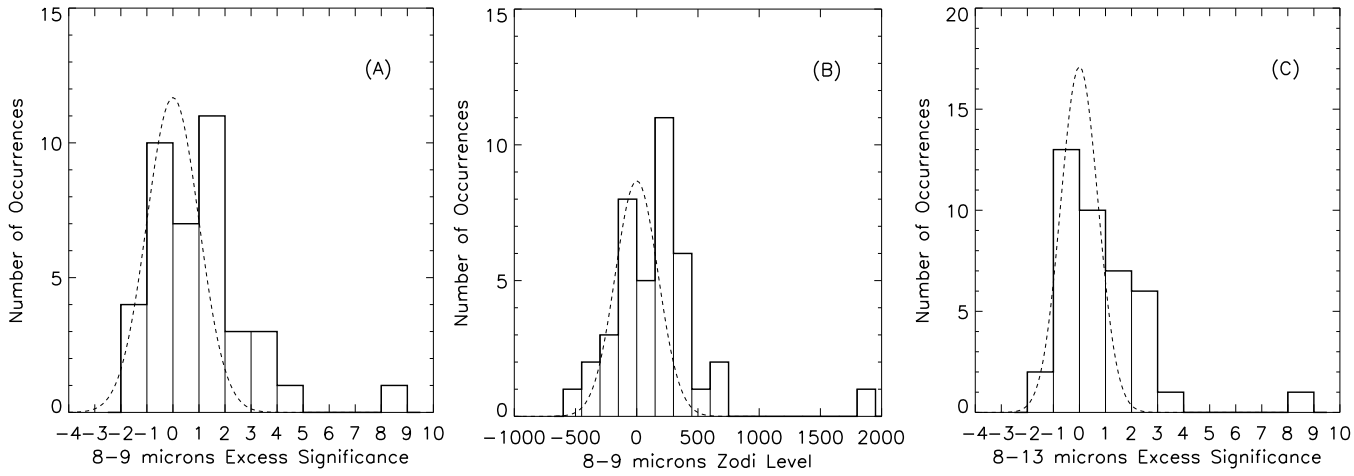

Fig. 3.— Statistical analysis. Histograms derived from the KIN measurements of 40 "effectively single" stars. Panel A: Histogram of the 8 to 9 μm excess significance. The observed histogram is highly asymmetric and obviously skewed towards positive excesses, with 5 stars showing excesses detected at the $> 3\sigma$ level. Panel B: Histogram of exo-zodi levels (expressed in solar zodi units, 150 zodis per bin) derived from the KIN 8 to 9 μm measurements. The observed histogram is again asymmetric and obviously skewed towards zodi levels higher than the average measurement error of 200 zodis rms, showing a large number of measurements between 150 and 450 zodis. Panel C: Histogram of broad-band 8 to 13 μm excess significance. Broad-band excess error bars and significance are estimated assuming full correlation between the 10 spectral channels, which is the worse case scenario. The observed histogram is also asymmetric with a tail extending towards positive excesses, 2 stars showing excesses detected at the $> 3\sigma$ level and 6 more above 2σ. For each plot, the dashed line indicates for comparison the instrumental noise distribution derived from the data, assuming gaussian behavior (see sections 4.1, 4.2 & 4.3 for details).

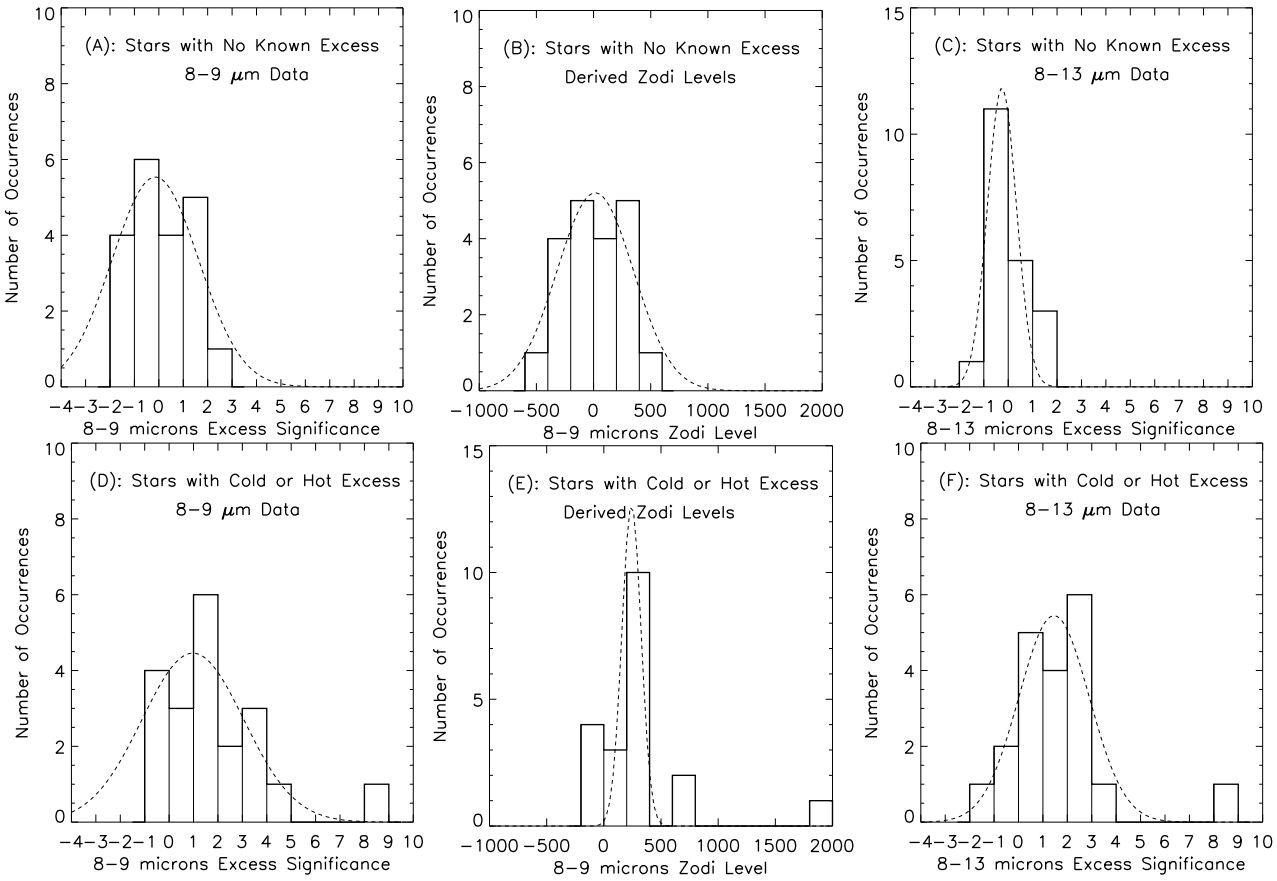

Fig. 4.— Comparing KIN results for stars with no infrared excess previously known (top panels) and stars with a cold (FIR) or hot (NIR) infrared excess previously detected (bottom panels). Each sub-group is composed of 20 stars. Panels A & D: histograms of the measured 8 to 9 μm excess significance. Panels B & E: histograms of exo-zodi levels derived from the 8 to 9 μm measurements, where each bin is 200 solar zodis wide. Panels C & F: histograms of the measured 8 to 13 μm excess significance. η Crv appears as a clear outlier in all lower panels histograms, with a high excess significance (> 8) and the largest measured zodi level (1870 zodis). For all panels, the dashed lines indicate the best fit gaussian distribution to the data (ignoring η Crv for the lower panels fits). Stars with previously detected cold (FIR) or hot (NIR) excesses have observed distributions systematically shifted towards higher excess significance and zodi levels, with a high number of measurements concentrating between 200 and 400 solar zodis, and three above 600 zodis (panel E). They are also the only stars to show 8 to 9 μm excesses detected above 3σ (5 stars in panel D), or 8 to 13 μm excesses detected above 2σ (8 stars in panel F).

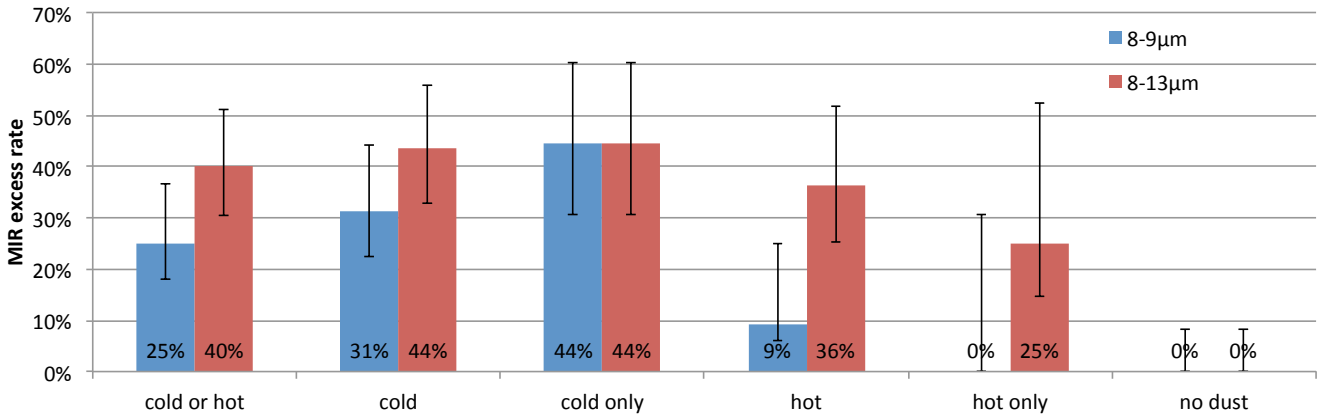

Fig. 5.— MIR excess rates measured by the KIN for stars with various types of infrared excess previously known (or lack of it). Between 8 and 9 μm, the excess rate is defined as the fraction of stars with a KIN excess significance greater than $3\,\sigma$, the most robust excess rate measurement derived from the KIN data. Between 8 and 13 μm, the excess rate is defined as the fraction of stars with a KIN broad-band correlated excess significance greater than $2\,\sigma$. The strongest correlation is seen with stars having a cold excess detected at FIR wavelengths (70 μm or longer). The (asymmetric) statistical uncertainty on the excess rate results from a numerical integration of the binomial distribution. See section 4.5 for details.

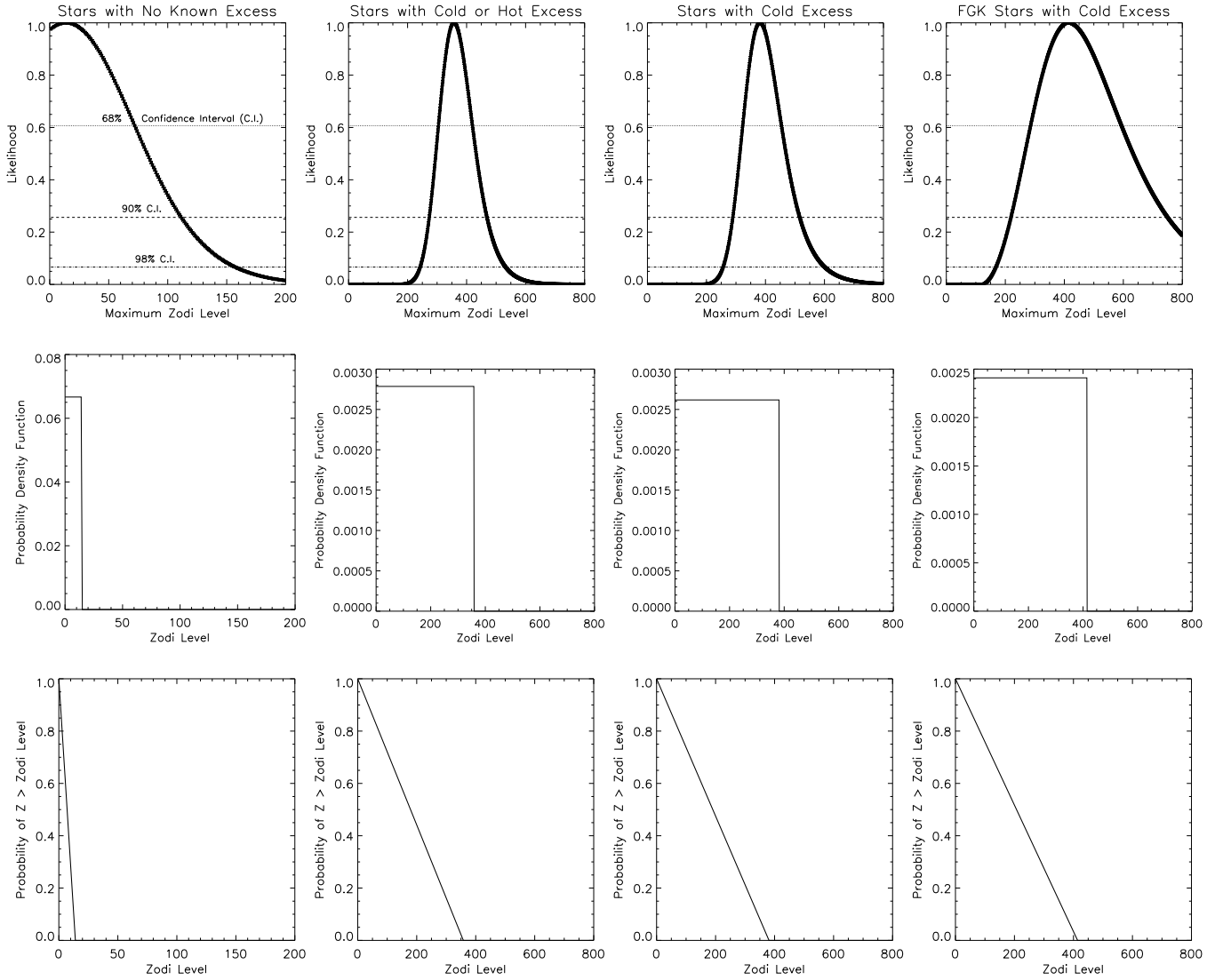

Fig. 6.— Results of maximum likelihood estimation assuming a uniform zodi distribution between 0 and some maximum zodi value Z_{max}, which is the only free parameter. Each column shows the results found for a different group of targets. From left to right: stars with no previously known excess (20 targets, Group 1), stars with previously known (hot or cold) infrared excess (19 targets, Group 2), stars with a known FIR (cold) excess (15 targets, Group 2a), and solar-type stars with a known FIR (cold) excess (8 targets, Group 2b). Top row: measured likelihood (normalized to its max) as a function of distribution parameter Z_{max}. Horizontal lines indicate confidence intervals at 68% (dotted lines), 90% (dashed lines) and 98% (dash-dotted lines) for the distribution parameter. For one-sided confidence intervals, i.e, lower or upper bounds, these same lines correspond to 84%, 95% and 99% confidence levels, respectively. Middle and bottom rows: resulting maximum likelihood distributions and cumulative fractions given the data. Note the smaller range of zodi levels displayed in the first column panels.

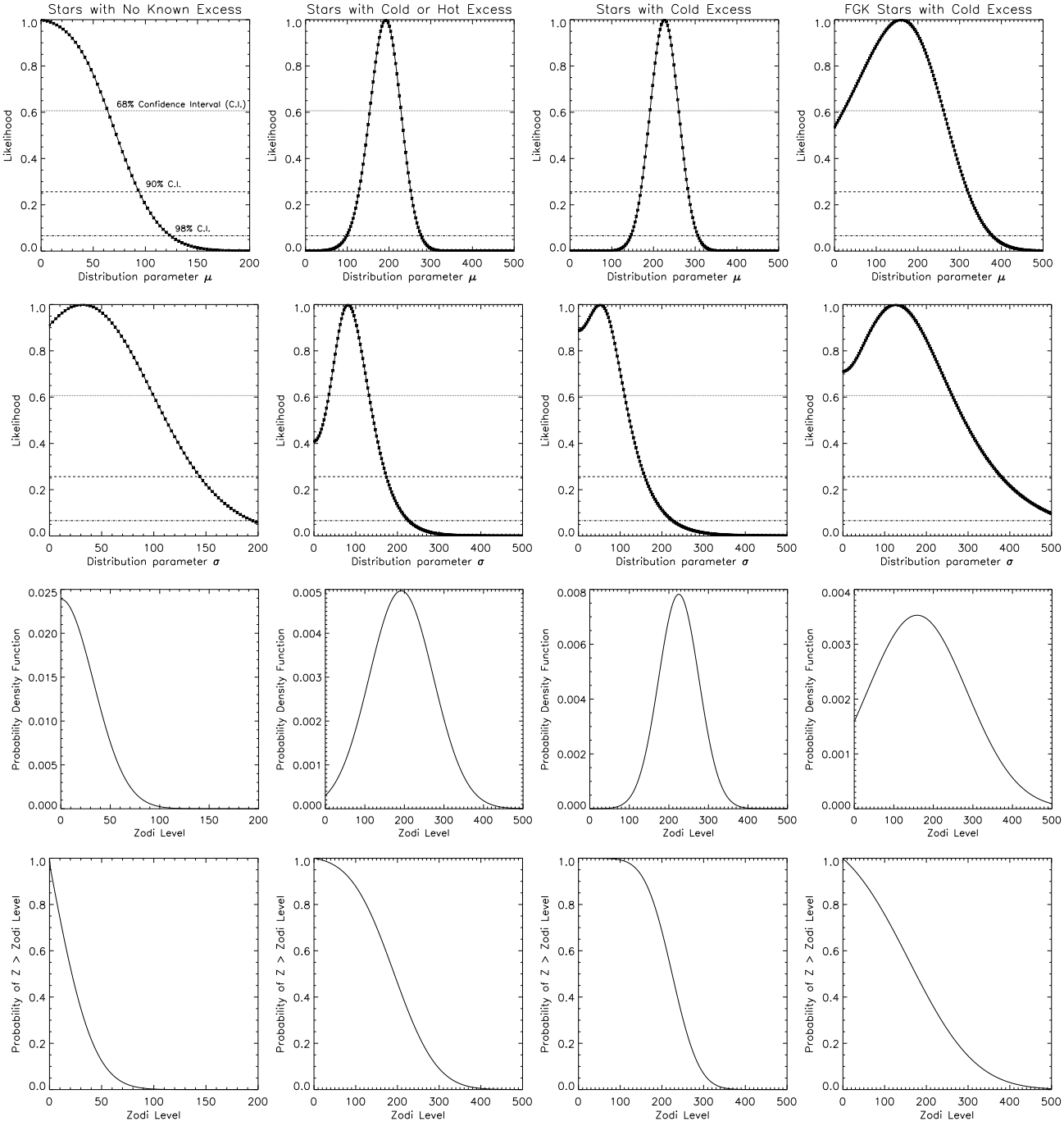

Fig. 7.— Results of maximum likelihood estimation assuming a truncated gaussian zodi distribution with parameters μ and σ, respectively the mean and standard deviation of the parent gaussian distribution. Each column shows the results found for a different group of targets, as defined in Figure 6 and indicated at the top. Top two rows: measured likelihood (normalized to its max) as a function of distribution parameter values. Horizontal lines indicate confidence intervals at 68% (dotted lines), 90% (dashed lines) and 98% (dash-dotted lines) for the distribution parameter. For one-sided confidence intervals, i.e, lower or upper bounds, these same lines correspond to 84%, 95% and 99% confidence levels, respectively. Bottom two rows: resulting maximum likelihood distributions and cumulative fractions. Note the smaller range of zodi levels displayed in the first column panels.

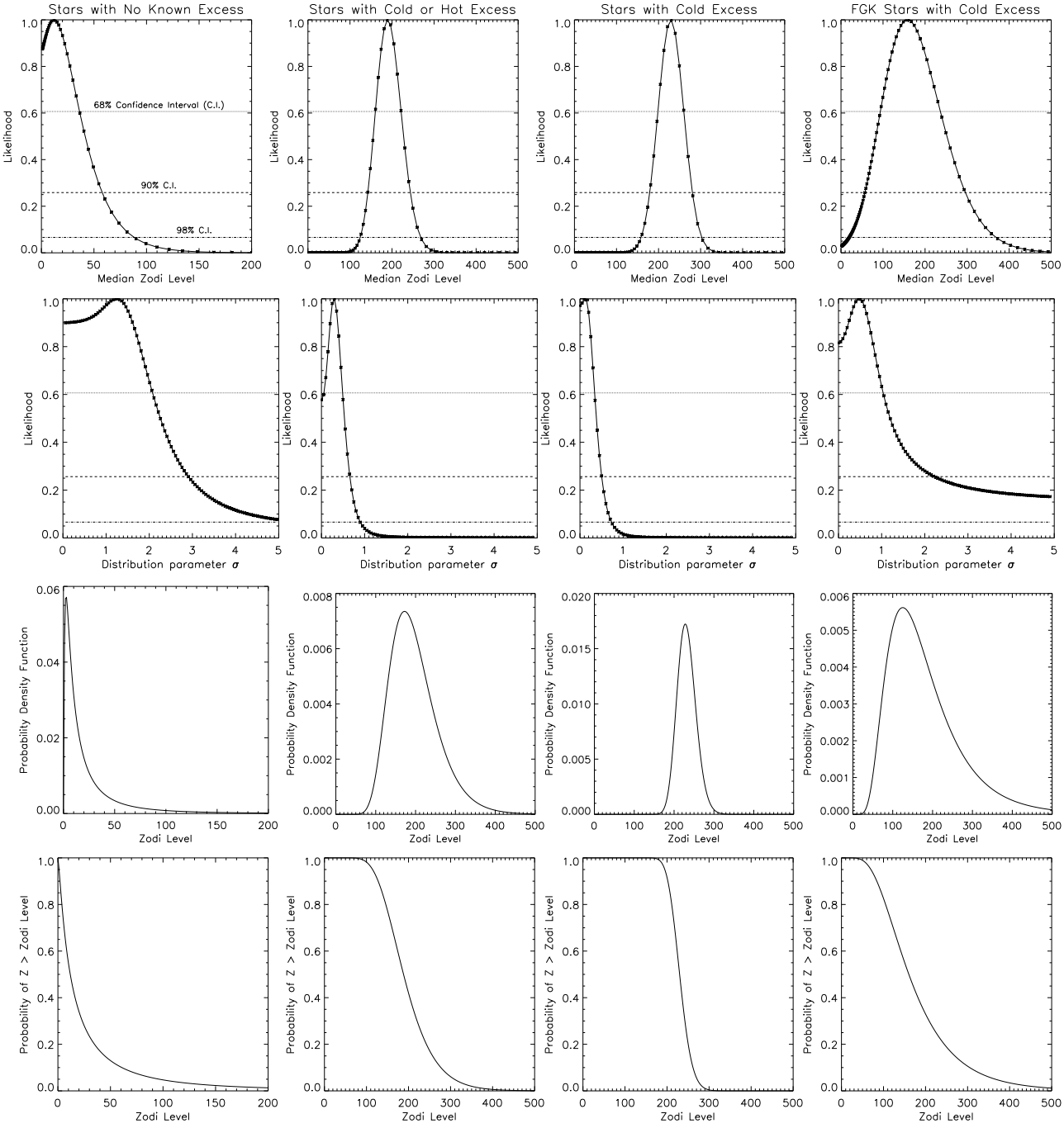

Fig. 8.— Results of maximum likelihood estimation assuming a log-normal zodi distribution with parameters μ and σ. Each column shows the results found for a different group of targets, as defined in Figure 6 and indicated at the top. Top two rows: measured likelihood (normalized to its max) as a function of distribution parameter values. The top row is actually plotted as a function of the distribution median value, which is the exponential of the μ parameter. Horizontal lines indicate confidence intervals at 68% (dotted lines), 90% (dashed lines) and 98% (dash-dotted lines) for the distribution parameter. For one-sided confidence intervals, i.e, lower or upper bounds, these same lines correspond to 84%, 95% and 99% confidence levels, respectively. Bottom two rows: resulting maximum likelihood distributions and cumulative fractions. Note the smaller range of zodi levels displayed in the first column panels.

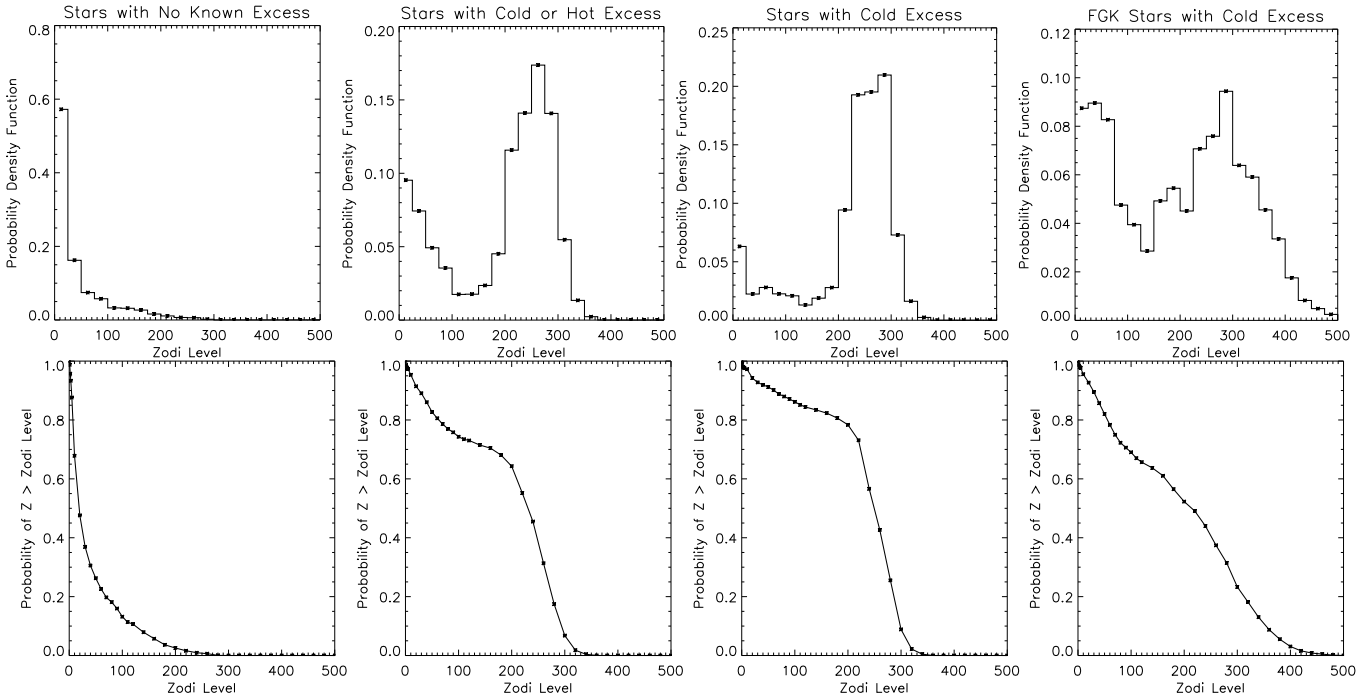

Fig. 9.— Zodi level distributions and cumulative fractions derived for different sub-groups of stars, using the iterative blind deconvolution method. Histograms bin size is 25 zodis. Each column shows the results found for a different group of targets, as defined in Figure 6 and indicated at the top. From left to right: stars with no previously known excess (20 targets, Group 1), stars with previously known (hot or cold) infrared excess (19 targets, Group 2), 15 stars with a known FIR (cold) excess (15 targets, Group 2a), and solar-type stars with a known FIR (cold) excess (8 targets, Group 2b). Note the widely different distributions derived for stars with a cold excess vs stars with no previously known excess.

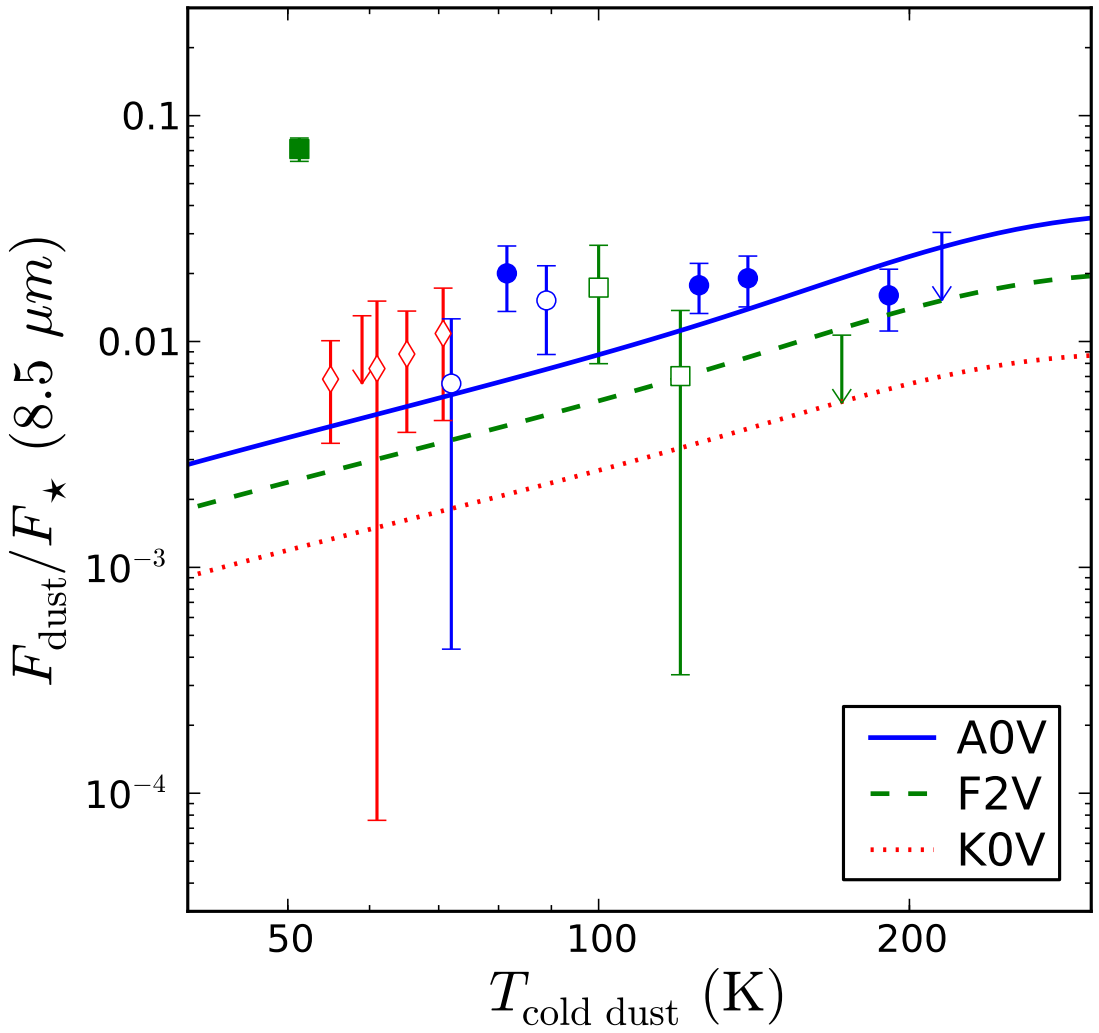

Fig. 10.— KIN measurements of MIR relative disk flux ratio and comparison with a P-R drag / collisions model. Data are for 16 targets with cold dust previously detected in the FIR (15 stars of group 2a, plus the top left outlier η Crv). Circles: A stars; squares: F stars; diamonds: G and K stars. Stars with a detected KIN excess are indicated with closed symbols. Error bars are $\pm$ 1σ, except for "negative excess flux measurements" which are given as 3 σ upper limits and indicated by down facing arrows (A star: δ UMa, F star: η Lep and G star: τ Ceti). The three model curves show the fractional excess expected for stars of different spectral types (solid line: A0V, dashed line: F2V, dotted line: K0V) assuming that a cold outer belt feeds dust to the inner system through the joint effect of P-R drag and grain collisions (Wyatt 2005). In this model, the MIR disk flux depends only weakly on the optical depth of the outer disk, as long as it is higher than $\simeq 10^{-5}$, which is the case of all stars considered here. An optical depth of 10^{-4} is assumed for these plots. Most disk fractional fluxes concentrate between $\simeq$ 0.5% and 2%. Observed fluxes are higher than predicted by the model for G/K stars, but only at the 2σ level (error bars are highly asymmetric because of the log-scale). See section 4.7.1 for further details.

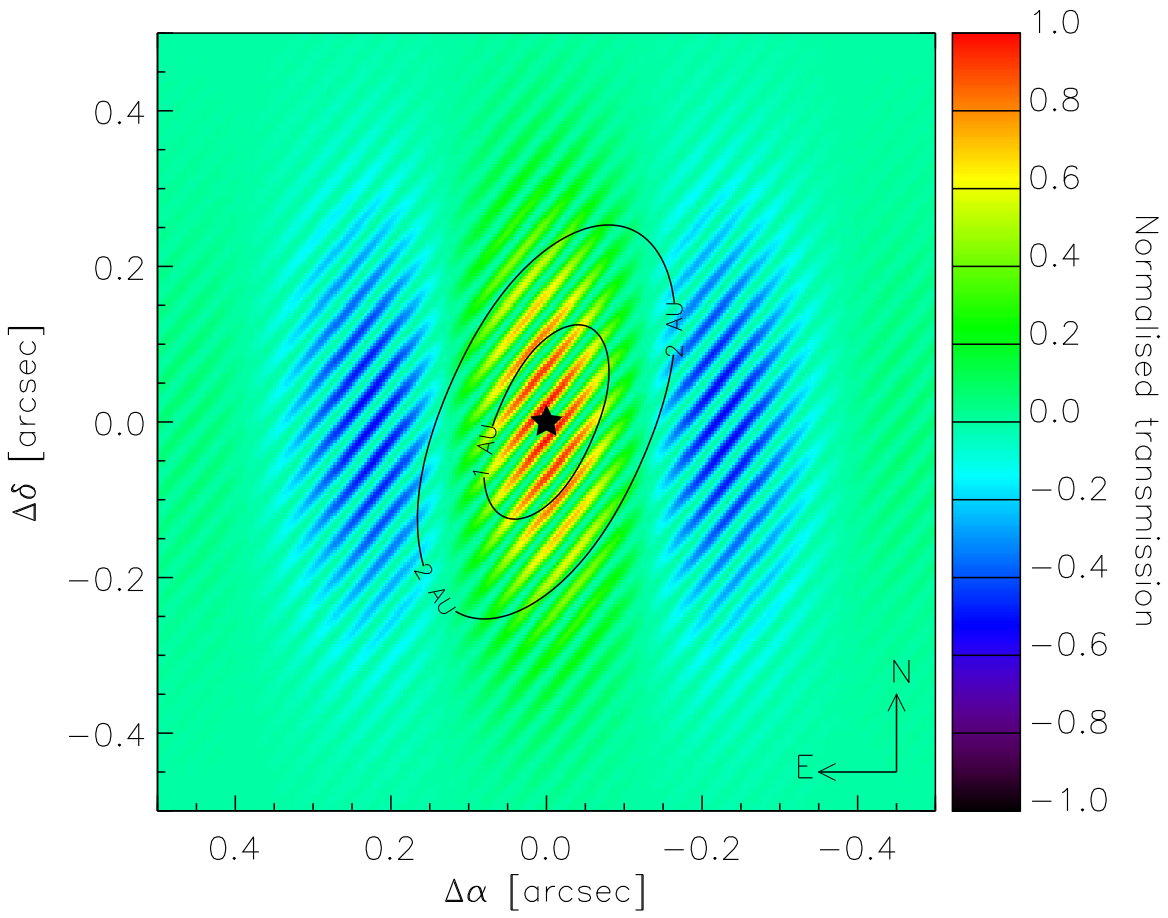

Fig. 11.— Keck Nuller sky transmission at 10 μm, when observing Fomalhaut at meridian transit on July 17, 2008 (Julian date: 2454664.07, projected baseline: 67.8 m, azimuth: 49.°6). North is up, East is to the left. High frequency fringes correspond to the long baseline separating the telescopes. The low frequency modulation is produced by interference between the sub-apertures of a single Keck telescope ("cross combiner" fringes); these fringes are aligned with the East-West direction when observing a star at transit. The contours indicate inner regions of the Fomalhaut system ($i = 66°$, PA $= 156°$), showing that the KIN is sensitive to dust emission in the 0.05 to 2 AU range at the star distance. As noted before (Mennesson et al. 2013), a curious effect of the KIN 4-beam combination is that for emission sources extending further out than λ/b in the direction of the cross-combiner baseline b ($\simeq 4\,m$), some regions will contribute a "negative leakage", i.e., effectively decrease the observed null depth. This is illustrated by the two blue areas of negative transmission centered around ± 0.25" in RA.

Table 1. Targets properties and observing log.

HD	Star	Spectral Type	Object Type	$L_{star}/L_{\odot}$	$R_{star}/R_{\odot}$	T_{star} (K)	F_{star} (Jy)	LD Diam (mas)	IWA (AU)	OWA (AU)	R_{300K} (AU)	Nc	Dates (UT)	Ns
432	β Cas	F2IV	ecold	27.3	3.4	7079	15.3	2.027 ± 0.122	0.10	3.4	**5.2**	2	2008/08/17	3
N/A	η Cas A	G3	···	1.3	1.0	6087	9.8	1.894 ± 0.114	0.04	1.2	1.1	2	2010/09/22	3
9826	υ And	F9V	···	3.3	1.6	6120	3.9	1.021 ± 0.060	0.08	2.7	1.8	1	2008/11/12	2
10476	107 Psc	K1V	···	0.4	0.8	5180	2.6	1.067 ± 0.064	0.04	1.5	0.7	2	2008/10/13	2
10700	τ Ceti	G8V	eboth	0.5	0.8	5344	11.8	2.015 ± 0.023	0.02	0.7	0.7	5	2008/10/14	4
													2008/10/15	2
13161	β Tri	A5III	bin3	71.0	4.4	8020	4.7	1.050 ± 0.100	0.23	7.8	8.4	2	2008/08/18	1
13974	δ Tri	G0V	bin3	1.1	1.0	5860	2.7	1.105 ± 0.111	0.07	2.2	1.0	2	2008/11/13	2
16895	θ Per	F7V	···	2.2	1.2	6320	4.0	1.086 ± 0.056	0.07	2.2	1.5	3	2009/01/11	2
													2009/01/12	1
19373	ι Per	F9V	···	2.2	1.4	5890	4.7	1.086 ± 0.056	0.06	2.1	1.5	4	2009/01/11	1
20630	κ-1 Cet	G5V	···	0.8	1.0	5620	2.7	0.895 ± 0.070	0.05	1.8	0.9	2	2009/01/10	1
22049	ϵ Eri	K2V	ecold	0.3	0.7	5084	12.2	2.126 ± 0.131	0.02	0.6	0.5	3	2008/10/13	2
													2008/10/14	3
													2009/01/13	1
22484	10 Tau	F8V	eboth	3.0	1.6	5981	3.7	1.130 ± 0.068	0.08	2.8	1.7	3	2011/02/14	2
30652	1 Ori	F6V	···	2.6	1.3	6450	7.9	1.409 ± 0.050	0.05	1.6	1.6	3	2008/02/17	3
													2008/02/18	1
34411	λ Aur	G1IV-V	···	1.7	1.3	5820	2.7	0.940 ± 0.056	0.08	2.5	1.3	2	2009/01/12	1
38393	γ Lep	F6V	···	2.3	1.2	6410	5.9	1.871 ± 0.112	0.05	1.8	1.5	3	2009/01/10	1
													2009/01/13	1
38678	ζ Lep	A2IV-V	ecold	14.0	1.5	9772	2.6	0.670 ± 0.140	0.13	4.3	3.7	5	2008/11/12	2
													2009/01/9	1
													2009/01/12	1
													2009/01/13	1
													2011/02/14	1
39587	χ-1 Ori	G0V	bin1	1.0	1.0	5930	3.6	1.124 ± 0.057	0.05	1.7	1.0	4	2009/01/10	2
													2009/01/13	2
40136	η Lep	F2V	eboth	4.6	1.5	6900	3.7	0.987 ± 0.059	0.09	3.0	2.1	4	2009/01/9	3
													2009/01/10	1
													2009/01/13	1
56537	λ Gem	A3V	ehot	27.8	2.0	9380	2.6	0.644 ± 0.006	0.19	6.2	5.3	2	2010/09/22	2
88230	NSV 4765	K8V	···	0.1	0.8	3920	3.1	1.238 ± 0.054	0.03	1.0	0.4	2	2009/01/10	1
95128	47 UMa	G1V	···	1.6	1.2	5860	2.0	0.774 ± 0.073	0.08	2.8	1.2	4	2009/01/10	1
													2009/01/11	1
95418	β Uma	A1V	ecold	63.0	3.0	9377	6.0	1.078 ± 0.065	0.15	4.9	**7.9**	2	2008/05/26	2
													2008/05/27	2
95735	HIP 54035	M2V	···	0.025	0.3	3730	3.2	1.439 ± 0.050	0.02	0.5	0.1	1	2008/04/14	2
													2009/01/10	1
102647	β Leo	A3V	eboth	15.0	1.7	8500	9.1	1.339 ± 0.087	0.07	2.2	**3.9**	2	2008/02/18	2
													2008/04/16	3
													2009/01/11	1
102870	β Vir	F9V	···	3.4	1.7	6080	6.6	1.431 ± 0.086	0.07	2.2	1.9	3	2008/02/17	2
													2008/02/18	4
106591	δ Uma	A3V	ecold	14.0	1.4	9480	3.0	0.823 ± 0.049	0.15	4.9	3.7	4	2008/04/16	3
													2009/01/10	1
109085	η Crv	F2V	ecold	4.7	1.5	6870	2.5	0.833 ± 0.050	0.11	3.6	2.2	5	2008/04/17	1
													2008/05/24	3
114710	β Com	G0V	···	1.3	1.1	5960	3.8	1.071 ± 0.058	0.05	1.8	1.2	3	2008/02/16	3
115617	61 Vir	G7V	ecold	0.9	1.0	5577	3.2	1.164 ± 0.116	0.05	1.7	0.9	3	2009/01/12	3
117176	70 Vir	G5V	ecold	3.1	1.9	5545	2.8	0.953 ± 0.062	0.11	3.6	1.8	5	2008/04/15	1
													2008/04/17	3
													2009/01/13	2
120136	τ Boo	F6IV	bin1	3.0	1.4	6370	2.5	0.864 ± 0.066	0.09	3.1	1.7	2	2008/05/25	3
													2008/05/27	2
131977	KX Lib	K4V	···	0.3	0.8	4570	3.1	1.490 ± 0.089	0.04	1.2	0.5	2	2008/05/26	2
142091	κ Crb	K1IV	eboth	12.9	5.0	4877	5.5	1.550 ± 0.093	0.19	6.2	3.6	1	2011/06/25	2
142860	γ Ser	F6IV	···	2.7	1.4	6370	4.7	1.161 ± 0.055	0.07	2.2	1.7	2	2008/04/16	3
													2008/04/17	2
161868	γ Oph	A0V	ecold	21.9	1.9	9030	1.8	0.630 ± 0.063	0.17	5.8	4.7	4	2008/07/16	3
													2008/07/17	3
165341	70 Oph	K0V	···	0.6	1.0	5140	9.8	2.037 ± 0.122	0.03	1.0	0.8	1	2008/08/17	2
													2008/08/18	2
172167	Vega	A0V	eboth	40.1	2.4	9602	53.9	3.306 ± 0.030	0.05	1.5	**6.3**	9	2008/05/27	4
													2008/07/14	1
													2008/07/15	4
													2008/08/15	2
													2008/08/16	7
177724	ζ Aql	A0V	ehot	39.0	2.3	9620	3.6	0.888 ± 0.136	0.15	5.1	**6.2**	2	2010/09/22	3
187642	Altair	A7V	ehot	10.6	1.6	6900	46.1	3.640 ± 0.030	0.03	1.0	**3.3**	4	2008/05/25	2
													2008/05/26	3
													2011/06/25	3

Table 1—Continued

HD	Star	Spectral Type	Object Type	$L_{star}/L_{\odot}$	$R_{star}/R_{\odot}$	T_{star} (K)	F_{star} (Jy)	LD Diam (mas)	IWA (AU)	OWA (AU)	R_{300K} (AU)	Nc	Dates (UT)	Ns
201091	61 Cyg A	K5V	bin3	0.2	0.7	4300	6.7	1.775 ± 0.013	0.02	0.7	0.4	2	2008/08/17	3
203280	α Cep	A7IV	ehot	17.0	2.3	7740	9.3	1.577 ± 0.095	0.09	3.0	**4.1**	2	2010/09/21	2
210027	ι Peg	F5V	bin2	3.3	1.4	6540	4.8	1.070 ± 0.100	0.07	2.4	1.8	2	2008/07/14	2
216956	α Psa	A4V	eboth	16.6	1.8	8590	21.9	2.223 ± 0.022	0.05	1.5	**4.1**	3	2008/07/16	4
													2008/07/17	4
222368	ι Psc	F7V	···	3.3	1.6	6240	3.9	1.062 ± 0.135	0.08	2.8	1.8	4	2008/10/13	2
19356	β Per	B8V	bin4	98	3.0	11400	9.4	1.350 ± 0.100	0.07	2.2	11.7	3	2008/10/15	3
													2008/10/16	2
83808	14 Leo	A5V	bin4	11.6	1.7	8180	5.3	1.347 ± 0.081	0.24	8.0	3.4	4	2008/02/16	2
													2008/02/17	3
													2008/04/14	4
139006	α Crb	F0V	bin4	5.8	1.5	7300	6.9	1.202 ± 0.056	0.14	4.6	2.4	4	2008/04/14	4
													2008/04/15	3
													2008/07/13	4

Note. — ist of KIN targets sorted by increasing right ascension. Object Type: indicates any peculiarity about the target. "bin1" : binary system with companion outside of KIN filed of view. "bin2" : binary system with companion of known properties within the KIN FOV and no obvious signature in the null measurements. "bin3" : binary system with companion of unknown brightness and no obvious signature within the KIN FOV. "bin4" : binary system with companion inside the KIN FOV and some obvious signature in the null measurements. No zodiacal level estimation was possible for these 3 "bin4" stars, which are listed separately at the end of the table. "ecold": cold excess previously detected at MIR or FIR wavelengths. "ehot": hot excess previously detected in the NIR. "eboth": both cold and hot excess previously detected. F_{star}: 10 μm stellar flux in Jy. LD Diam: stellar limb darkened diameter in mas. IWA/ OWA: KIN inner and outer working angles (in AU). R_{300K}: minimum distance for 300 K dust (in AU). N_c total number of calibrator stars used. N_s: total number of null data sequences recorded.

Table 2. KIN Results Summary in the context of other IR excess measurements

Star	E_{8-9}	σ_{8-9}	S_{8-9}	Zodis	E_{8-13}	σ_{8-13}^{uncor}	S^{uncor}	σ_{8-13}^{cor}	S^{cor}	NIR/MIR/FIR Excesses	T_{cold} (K)
η Crv	2.7e-02	3.2e-03	8.35	1813 ± 209	4.4e-02	2.0e-03	22.30	5.1e-03	8.69	$N^a/Y^b/Y^c$	50
β UMa	7.1e-03	1.8e-03	4.02	327 ± 80	6.4e-03	9.2e-04	7.00	2.5e-03	2.54	$N^a/Y^b/Y^{c,x}$	140
β Leo	5.6e-03	1.4e-03	3.96	291 ± 73	4.2e-03	6.8e-04	6.17	1.9e-03	2.21	$Y^a/Y^b/Y^{c,d}$	125
ζ Lep	5.9e-03	1.8e-03	3.30	243 ± 73	9.6e-03	1.2e-03	8.31	3.1e-03	3.12	$N^a/Y^b/Y^e$	190
γ Oph	8.7e-03	2.8e-03	3.08	306 ± 99	1.1e-02	1.9e-03	5.96	5.1e-03	2.22	$N^a/Y^f/Y^f$	80
Vega	2.1e-03	8.9e-04	2.30	297 ± 124	2.2e-03	3.4e-04	6.32	1.0e-03	2.13	$Y^a/Y^{e,g}/Y^e$	90
ϵ Eri	2.5e-03	1.2e-03	2.16	262 ± 117	1.8e-03	5.0e-04	3.61	1.4e-03	1.26	$N^a/Y^h/Y^h$	55
λ Aur	6.2e-03	3.0e-03	2.06	473 ± 226	5.6e-03	2.3e-03	2.40	6.2e-03	0.91	N/N/N	
10 Tau	7.6e-03	4.1e-03	1.84	614 ± 333	2.4e-03	3.2e-03	0.76	8.8e-03	0.28	Y^a/N/Y^i	100
70 Vir	4.0e-03	2.2e-03	1.84	397 ± 208	5.6e-03	1.3e-03	4.30	3.5e-03	1.60	$N^a/Y^j/Y^{k,l}$	65
61 Vir	5.1e-03	3.0e-03	1.70	381 ± 221	4.6e-03	2.5e-03	1.81	6.6e-03	0.69	N/$N^i/Y^{i,m}$	70
η Cas A	3.1e-03	2.0e-03	1.55	267 ± 172	3.3e-03	9.9e-04	3.30	2.7e-03	1.21	N^a/N/N	
Altair	2.1e-03	1.4e-03	1.50	247 ± 176	3.8e-03	5.1e-04	7.57	1.5e-03	2.55	$Y^a/N^n/N^o$	
τ Boo	3.1e-03	2.1e-03	1.46	208 ± 142	2.1e-03	1.7e-03	1.24	4.5e-03	0.47	N/N^p/N^q	
1 Ori	3.0e-03	2.1e-03	1.41	215 ± 151	1.7e-03	1.2e-03	1.38	3.4e-03	0.50	N^a/N/N	
KX Lib	3.5e-03	2.5e-03	1.38	326 ± 235	-1.1e-03	1.9e-03	-0.58	4.9e-03	-0.23	N/N/N	
β Com	5.8e-03	4.8e-03	1.20	389 ± 326	3.0e-03	2.2e-03	1.34	6.0e-03	0.50	N/N/N	
α Psa	1.5e-03	1.4e-03	1.05	118 ± 107	3.7e-03	5.4e-04	6.96	1.6e-03	2.34	$Y^r/Y^s/Y^t$	70
β Cas	2.1e-03	2.0e-03	1.03	226 ± 216	1.7e-03	7.7e-04	2.24	2.2e-03	0.77	N^a/N/Y^u	120
ζ Aql	3.6e-03	4.4e-03	0.82	137 ± 167	1.8e-03	1.7e-03	1.04	5.0e-03	0.36	Y^a/N/N	
κ Crb	3.5e-03	4.4e-03	0.80	625 ± 791	6.4e-03	2.2e-03	2.91	5.9e-03	1.08	Y^a/N/Y^v	60
ι Psc	2.4e-03	3.0e-03	0.79	183 ± 230	8.2e-03	1.7e-03	4.67	4.8e-03	1.71	N/N/N	
107 Psc	2.0e-03	3.0e-03	0.67	160 ± 236	8.3e-03	2.5e-03	3.39	6.8e-03	1.23	N^a/N/N	
61 Cyg A^*	1.3e-03	2.2e-03	0.60	127 ± 212	2.1e-03	1.0e-03	2.00	2.8e-03	0.74	N^a/N/N	
70 Oph A	1.2e-03	2.2e-03	0.56	136 ± 237	-1.1e-03	9.9e-04	-1.09	2.8e-03	-0.39	N^a/N/N	
47 UMa	1.4e-03	2.8e-03	0.50	105 ± 207	-1.8e-03	2.0e-03	-0.91	5.3e-03	-0.34	N/N/N	
α Cep	3.4e-04	2.0e-03	0.17	24 ± 144	9.1e-04	9.7e-04	0.93	2.7e-03	0.34	Y^a/N/N	
δ UMa	-2.7e-04	2.4e-03	-0.11	-15 ± 140	3.8e-03	1.4e-03	2.81	3.7e-03	1.05	$N^a/Y^e/\ Y^e$	215
HIP 54035	-3.9e-04	2.5e-03	-0.16	-53 ± 366	-2.6e-03	2.0e-03	-1.35	5.2e-03	-0.50	N/N/N	
η Lep	-5.6e-04	1.7e-03	-0.32	-34 ± 113	-3.9e-03	1.1e-03	-3.62	2.8e-03	-1.37	$Y^a/Y^p/Y^l$	170
υ And	-1.1e-03	3.1e-03	-0.34	-76 ± 226	-8.3e-04	1.9e-03	-0.43	5.2e-03	-0.16	N^a/N/N	
χ_1 Ori	-9.2e-04	2.7e-03	-0.34	-60 ± 190	-8.2e-04	1.3e-03	-0.63	3.6e-03	-0.23	N/N/N	
τ Ceti	-1.1e-03	2.1e-03	-0.53	-95 ± 180	-8.4e-04	1.2e-03	-0.68	3.3e-03	-0.25	Y^a/N/Y^w	60
θ Per	-1.6e-03	2.8e-03	-0.56	-112 ± 204	3.7e-04	1.7e-03	0.22	4.5e-03	0.08	N^a/N/N	
ι Peg*	-1.4e-03	2.5e-03	-0.57	-100 ± 173	-4.2e-03	1.2e-03	-3.38	3.4e-03	-1.24	N/N/N	
β Vir	-2.1e-03	3.0e-03	-0.70	-170 ± 243	-3.7e-04	1.2e-03	-0.31	3.3e-03	-0.11	N^a/N/N	
κ_1 Cet	-3.6e-03	3.6e-03	-0.98	-249 ± 255	-8.5e-03	2.3e-03	-3.67	6.1e-03	-1.39	N/N/N	
λ Gem	-3.0e-03	3.0e-03	-1.00	-139 ± 140	-4.1e-03	2.3e-03	-1.80	6.1e-03	-0.67	Y^a/N/N	
$\delta\ Tri^*$	-3.7e-03	3.0e-03	-1.24	-298 ± 242	-6.6e-03	1.9e-03	-3.44	4.5e-03	-1.46	N/N/N	
$\beta\ Tri^*$	-6.5e-03	4.7e-03	-1.39	-436 ± 316	-7.1e-04	2.4e-03	-0.30	6.2e-03	-0.11	N/N/Y^o	90
NSV 4765	-4.6e-03	3.0e-03	-1.53	-477 ± 316	-3.1e-03	2.3e-03	-1.37	6.3e-03	-0.50	N/N/N	
γ Lep	-3.0e-03	1.8e-03	-1.67	-205 ± 127	-1.1e-03	9.0e-04	-1.23	2.4e-03	-0.46	N/N/N	
ι Per	-4.5e-03	2.5e-03	-1.82	-338 ± 188	-2.5e-04	1.4e-03	-0.18	3.7e-03	-0.07	N/N/N	
γ Ser	-4.4e-03	2.3e-03	-1.87	-304 ± 164	-3.3e-03	1.3e-03	-2.47	3.7e-03	-0.90	N^a/N/N	

Note. — Columns description. Star: targets observed by the KIN, *sorted by decreasing excess significance* in the 8 to 9 μm bin (S_{8-9}). *: targets with companions within KIN field of view (see section 3.3); E_{8-9}: 8 to 9 μm excess leak; σ_{8-9}: 8 to 9 μm excess leak uncertainty; 8 to 9 μm excess significance $S_{8-9} = (E_{8-9}/\sigma_{8-9})$; E_{8-13}: 8 to 13 μm excess leak ; σ_{8-13}^{uncor}: 8 to 13 μm excess leak uncertainty assuming uncorrelated spectral channels; $S^{uncor} = (E_{8-13}/\sigma_{8-13}^{uncor})$: 8 to 13 μm excess significance in uncorrelated case ; σ_{8-13}^{cor}: 8 to 13 μm excess leak uncertainty assuming fully correlated spectral channels; $S^{cor} = (E_{8-13}/\sigma_{8-13}^{cor})$: 8 to 13 μm excess significance in fully correlated case; "NIR/MIR/FIRμm excess" indicates whether a circumstellar excess has been reported in the NIR around 2.2 μm (^{a}: Absil et al. (2013)),

in the MIR (defined here as "any wavelength between 15 and 35 μm"), or in the FIR (anywhere between 70 and 160 μm); T_{cold} is the outer cold dust temperature derived from the MIR/FIR excesses when available, assuming black-body emission at a single radius. [b]: Chen et al. (2006), [c]: Matthews et al. (2010), [d]: Churcher et al. (2011), [e]: Su et al. (2006), [f]: Su et al. (2008), [g]: Su et al. (2013), [h]: Backman et al. (2009), [i]: Trilling et al. (2008), [j]: Bryden et al. (2009), [k]: Dodson-Robinson (2011), [l]: Eiroa et al. (2013), [m]: Wyatt et al. (2012), [n]: Rieke et al. (2005), [o]: Gaspar et al. (2013), [p]: Lawler et al. (2009), [q]: Beichman et al. (2006b), [r]: Absil et al. (2009), [s]: Stapelfeldt et al. (2004), [t]: Acke et al. (2012), [u]: Rhee et al. (2007), [v]: Bonsor et al. (2013), [w]: Habing et al. (2001), [x]: Booth et al. (2013).

Table 3. Summary of 8 to 9 μm excess rates measured as a function of spectral type and previously detected infrared excesses.

	A	F	G	K/M	Total
Stars with Cold or Hot Excess	4/11	1/4	0/3	0/2	5/20
Stars with Cold Excess	4/7	1/4	0/3	0/2	5/16
Stars with Cold Excess only	3/4	1/2	0/2	0/1	4/9
Stars with Hot Excess	1/7	0/2	0/1	0/1	1/11
Stars with Hot Excess only	0/4	none	none	none	0/4
Stars with No Known Excess	none	0/9	0/6	0/5	0/20
Overall Sample	4/11	1/13	0/9	0/7	5/40

Note. — A cold excess corresponds to a FIR excess detected anywhere between 70μm and 160 μm with Spitzer and/or Herschel (same as Table 2). A hot excess corresponds to an excess reported in the NIR around 2.2 μm (Absil et al. 2009, 2013).

Table 4. Median Zodi Levels

Distribution Type	Group 1 Stars with No Known Excess	Group 2 Stars with Cold or Hot Excess	Group 2a Stars with Cold Excess	Group 2b FGK Stars with Cold Excess
Uniform	7 [0-56]	177 [137 - 234]	190 [145 - 259]	207 [110 - 375]
Truncated Gaussian	20	190	227	160
Log-normal	12 [0 - 60]	190 [142 - 242]	230 [178 - 280]	160 [60 - 296]
from Blind Deconvolution	18	240	250	220

Note. — Median zodi values derived for 4 different sub-groups of stars observed by the KIN assuming different underlying distributions. Group 1: 20 solar type stars with no previously known IR excess of any kind; Group 2: 19 stars with previously known infrared excess (hot or cold); Group 2a: 15 stars with a known FIR (cold) excess. Group 2b: 8 FGK stars with a with a known FIR (cold) excess. In all cases, the most likely median zodi value is quoted, together with its 90% confidence interval when available. One-sided bounds have a 95% confidence level, meaning that in the log-normal case for instance, and with 95% confidence, Group 1 median zodi level is smaller than 60 solar zodis while that of Group 2a is higher than 178 solar zodis.

Table 5. Excess leaks measured as a function of wavelength for the 5 stars showing an excess in the 8 to 9 μm bin.

Star	Date (UT)	u (m)	v (m)	xs_1 (%)	xs_2 (%)	xs_3 (%)	xs_4 (%)	xs_5 (%)	xs_6 (%)	xs_7 (%)	xs_8 (%)	xs_9 (%)	xs_{10} (%)	xs_{8-9} (%)
η Crv	4/17/08	56.31	62.34	2.80 ± 0.54	2.36 ± 0.58	5.26 ± 0.66	9.27 ± 0.90	9.48 ± 1.03	10.40 ± 1.42	12.01 ± 1.46	13.60 ± 2.36	2.82 ± 4.96	-0.34 ± 7.58	2.50 ± 0.41
η Crv	5/24/08	46.62	51.97	2.72 ± 0.38	4.03 ± 0.34	5.90 ± 0.47	8.29 ± 0.70	8.78 ± 0.68	9.56 ± 0.83	10.79 ± 1.10	10.28 ± 1.96	8.14 ± 2.58	11.12 ± 3.79	3.39 ± 0.23
η Crv	5/24/08	34.39	48.37	2.33 ± 0.41	2.63 ± 0.38	4.72 ± 0.53	4.02 ± 0.79	7.71 ± 0.84	8.45 ± 1.02	8.58 ± 1.26	5.68 ± 1.98	4.21 ± 3.90	-2.38 ± 4.07	2.46 ± 0.31
η Crv	5/24/08	25.69	46.83	2.92 ± 1.03	1.06 ± 1.15	5.91 ± 1.04	1.76 ± 1.81	2.94 ± 1.49	4.53 ± 1.68	7.44 ± 2.98	-0.31 ± 4.40	6.08 ± 8.01	-2.68 ± 7.94	1.96 ± 0.92
β Uma	5/26-27/08	26.94	76.28	0.61 ± 0.18	0.84 ± 0.18	0.54 ± 0.22	0.64 ± 0.32	0.58 ± 0.34	0.29 ± 0.36	0.53 ± 0.47	0.61 ± 0.65	1.21 ± 0.97	0.50 ± 1.58	0.71 ± 0.18
β Leo	2/18/08	54.86	64.81	1.46 ± 0.46	1.07 ± 0.24	0.76 ± 0.28	0.48 ± 0.30	0.47 ± 0.25	0.09 ± 0.30	1.02 ± 0.60	0.80 ± 0.70	1.97 ± 0.99	-1.47 ± 1.70	1.25 ± 0.33
β Leo	4/16/08	55.63	62.74	-0.15 ± 0.28	-0.09 ± 0.25	-0.47 ± 0.39	-0.20 ± 0.30	0.21 ± 0.31	-0.26 ± 0.53	-0.14 ± 0.65	0.51 ± 0.95	-0.81 ± 1.36	-0.64 ± 2.61	-0.12 ± 0.26
β Leo	1/11/09	52.10	55.93	0.67 ± 0.26	0.72 ± 0.21	0.53 ± 0.24	0.79 ± 0.44	0.56 ± 0.55	-0.20 ± 0.55	1.73 ± 0.81	-1.08 ± 1.43	2.10 ± 2.38	-4.48 ± 3.68	0.73 ± 0.20
ζ Lep	11/12/08	36.05	50.36	0.84 ± 0.67	0.63 ± 0.41	1.18 ± 0.79	1.62 ± 1.28	1.96 ± 1.15	2.49 ± 1.39	3.18 ± 0.87	3.13 ± 2.12	0.67 ± 2.58	3.95 ± 7.44	0.72 ± 0.53
ζ Lep	1/9-13/2009	45.65	54.44	0.37 ± 0.31	0.64 ± 0.23	1.15 ± 0.26	0.78 ± 0.47	1.46 ± 0.47	1.35 ± 0.60	3.19 ± 0.90	1.81 ± 1.18	0.34 ± 1.84	2.31 ± 3.82	0.55 ± 0.20
ζ Lep	2/14/2011	31.49	49.33	2.20 ± 1.44	0.68 ± 1.02	2.37 ± 1.27	2.61 ± 1.37	-1.75 ± 1.72	-0.49 ± 2.37	-5.94 ± 3.62	-0.66 ± 5.11	0.81 ± 7.39	-7.74 ± 10.49	1.19 ± 0.92
γ Oph	7/16-17/2008	43.65	64.79	0.98 ± 0.36	0.69 ± 0.35	0.90 ± 0.42	1.07 ± 0.77	1.03 ± 0.75	2.54 ± 0.85	3.27 ± 0.95	3.72 ± 1.68	5.23 ± 2.37	3.56 ± 2.90	0.87 ± 0.28

Note. — xs_{1-10}: excess leaks measured in each of the 10 KIN spectral channels, which have central wavelengths increasing from 8.25 to 12.75 μm by 0.5 μm increments. xs_{8-9} is the synthetic excess leak measured in the 8 to 9 μm channel.